Precipitation and Cloud Structures of Intense Rain during the 2013 Great Colorado Flood

KATJA FRIEDRICH, EVAN A. KALINA, AND JOSHUA AIKINS

Department of Atmospheric and Oceanic Sciences, University of Colorado Boulder, Boulder, Colorado

DAVID GOCHIS AND ROY RASMUSSEN

National Center for Atmospheric Research, Boulder, Colorado*

(Manuscript received 25 August 2014, in final form 20 March 2015)

ABSTRACT

Radar and disdrometer observations collected during the 2013 Great Colorado Flood are used to diagnose the spatial and vertical structure of clouds and precipitation during episodes of intense rainfall. The analysis focuses on 30 h of intense rainfall in the vicinity of Boulder, Colorado, during 2200–0400 UTC 11–13 September. The strongest rainfall occurred along lower parts of the Colorado Front Range at >1.6 km MSL and on the northern side of the Palmer Divide. The vertical structure of clouds and horizontal distribution of rainfall are strongly linked to upslope flow and low-level forcing, which resulted in surface convergence. During times of weak forcing, shallow convection produced rain at and below the melting layer through collision–coalescence and, to a lesser extent, riming. A mesoscale circulation interacting with the local terrain produced convective rainfall with high cloud tops that favored ice crystal production. During moderate forcing with cloud tops slightly exceeding the 0°C level, both cold- and warm-phase microphysical processes dominated. Less rain with weaker rainfall rates was observed over the higher-elevation stations compared to the lower-elevation stations across the foothills.

1. Introduction

The Great Colorado Flood in September 2013 was an unusual event, not only because of its duration and the amount of precipitation but also because of the atypical precipitation character for an early fall precipitation event in the Colorado Front Range (Fig. 1; Gochis et al. 2015). Large amounts of precipitation between 11 and 13 September occurred over very localized areas on the eastern slopes of the Colorado Rocky Mountains, such as the Colorado Front Range between Golden and Estes Park, and on the northern side of the Palmer Divide east of Longmont (Figs. 1a,b; Gochis et al. 2015). As shown in Gochis et al. (2015), many forecasting and nowcasting systems operated by the National Weather Service failed to correctly predict the duration, distribution, and amount of precipitation during this event. Some of the unusual characteristics of the event as summarized in Gochis et al. (2015) include 3 days of extreme rainfall (>400 mm accumulated between 11 and 16 September), a large concentration of small raindrops at the surface, and a large amount of precipitable water, most of which fell primarily along the Front Range and the lower foothills. Another unusual characteristic of the storm, which occurred over a high-elevation, midlatitude, continental interior region, was the low cloud base (~200 m AGL) and surface temperatures of about 15°C. Since the melting layer was ~2.7 km above the ground, the low cloud base provided a ~2.5-km-deep collision–coalescence zone, which is typical for warm rain in Hawaii but not for summertime precipitation in Colorado. Nevertheless, raindrops with small diameters ($d \sim 1$ mm) were frequently observed by surface disdrometers during the Colorado Flood [Fig. 10c in Gochis et al. (2015)].

* The National Center for Atmospheric Research is sponsored by the National Science Foundation.

Corresponding author address: Dr. Katja Friedrich, Dept. of Atmospheric and Oceanic Sciences, University of Colorado Boulder, UCB 311, Boulder, CO 80309.
E-mail: katja.friedrich@colorado.edu

DOI: 10.1175/JHM-D-14-0157.1

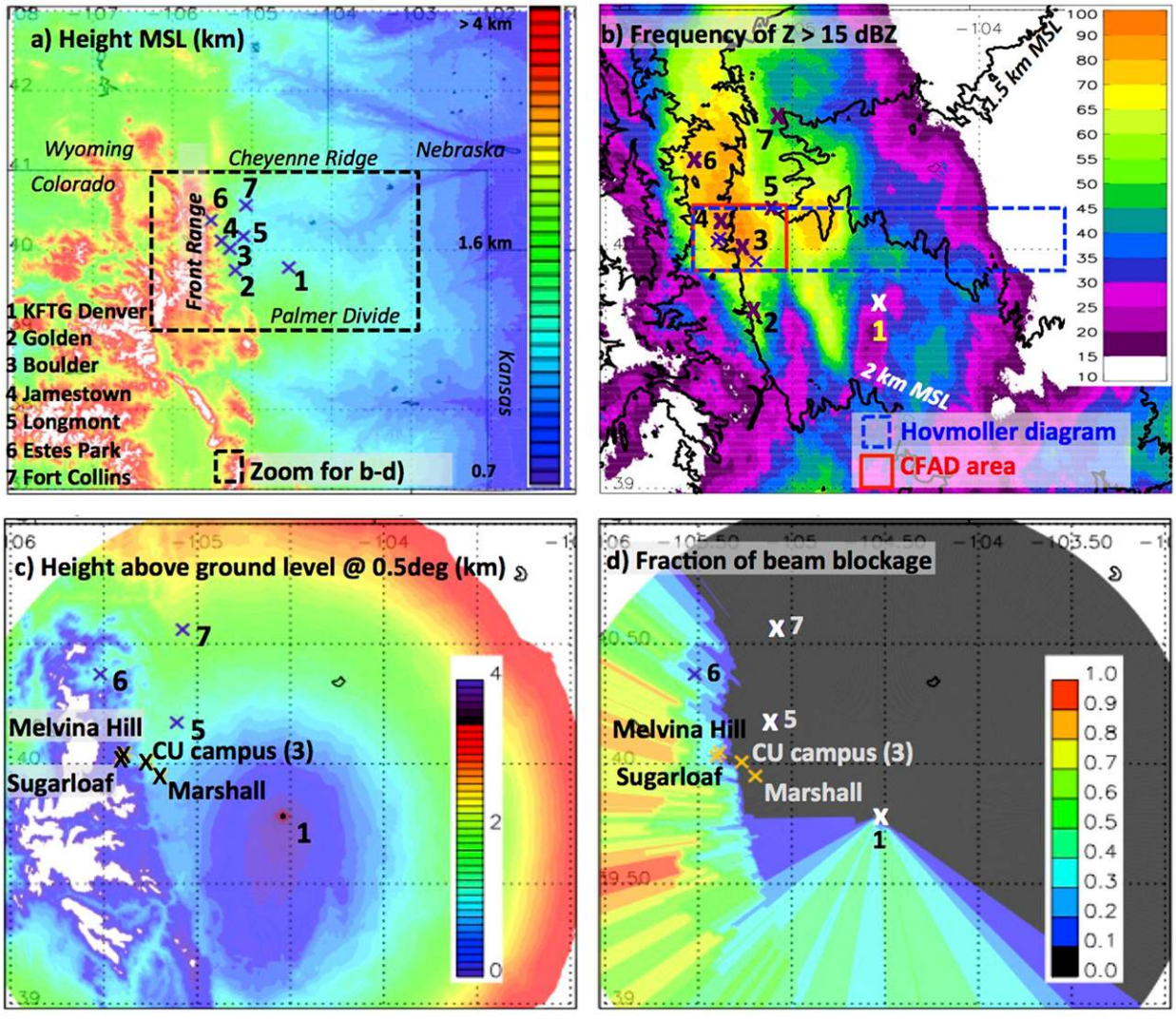

FIG. 1. (a) Topographic map, (b) frequency of $Z > 15$ dBZ between 2200 and 0400 UTC 11–13 Sep 2013 based on the Denver KFTG radar data, (c) height above ground level at 0.5° elevation angle, and (d) fraction of beam blockage for the lowest elevation angle of 0.5° up to 150-km range from the radar. The × signs approximate town and instrument locations at Marshall, CU campus, Melvina Hill, and Sugarloaf. Numbers are related to the name of the towns listed in (a). The black box in (a) outlines the boundary of the data shown in (b)–(d). Black lines in (b) denote height lines at 1.5, 2, 3, and 4 km MSL. Red and blue boxes in (b) highlight a special investigation area for the Hovmöller diagrams and CFAD analysis, respectively.

In this study, we broaden the analysis of precipitation and clouds presented in Gochis et al. (2015) and provide more insights on the spatial and temporal variation of clouds and precipitation and their vertical structure, especially during the most intense rainfall between 2200 UTC 11 September and 0400 UTC 13 September 2013. We analyze the role of the Colorado Front Range in influencing the distribution and amount of precipitation. We also investigate how differences in the vertical structure of clouds and precipitation, especially between lower-elevation and higher-elevation stations, affect the rainfall amount at the surface.

Heavy summertime precipitation along the Front Range occurs primarily during two periods, according to an analysis of the 300 heaviest precipitation events in Colorado since the 1800s by Petersen et al. (1999) and McKee and Doesken (1997). The first is from late May to early June with moderate widespread precipitation, embedded convection, and orographic enhancement. The second occurs from late July to early September and is dominated by localized thunderstorms. Most of the heaviest precipitation events occur as summertime convection and produce large amounts of rain over small spaces and time ranges that strongly impact mountain

communities and dense urban areas along the Front Range. These events often trigger flash floods and mudslides (Maddox et al. 1978; Caracena et al. 1979; Sveinsson et al. 2002; Godt and Coe 2007). Sometimes, these events occur in tandem with springtime snowmelt, which adds additional volume to the runoff (Petersen et al. 1999; Weaver et al. 2000). At the same time, heavy rainfall that occurs over burn scars left behind by wildfires can trigger dramatic increases in runoff and erosion (Benavides-Solorio and MacDonald 2001; Moody and Martin 2001; Wagenbrenner et al. 2006). Flood events in the Colorado Rocky Mountain region have been well documented and well studied (e.g., Hirschboeck 1991). The most devastating floods that occurred along the Front Range in the last century include the Big Thompson flash flood in July 1976 (Maddox et al. 1977, 1978) and the Fort Collins flash flood of July 1997 (Petersen et al. 1999). Contrary to most of the localized, short-lived flash flood events along the Colorado Front Range, the 2013 Great Colorado Flood was unusual in that rainfall occurred over many days with antecedent precipitation, causing over 1300 landslides, destroying over 150 miles of road, and forcing over 18 000 people to leave their homes (Table 2 in Gochis et al. 2015).

The 2013 Great Colorado Flood, which was caused by widespread stratiform precipitation with embedded convective cells, does not represent the climatological pattern expected in mid-September. Climatologically, moisture transported from the Gulf and subtropical Atlantic generates thunderstorms and intense precipitation between April and early September along the Front Range with dry conditions in September (Collins et al. 1991). However, similar to other flash flood events near the Front Range, the environment and the rainfall characteristics show similarities to tropical rainfall, with moist conditions throughout the troposphere, weak-to-moderate southwesterly midtropospheric winds, easterly winds at the surface, and a large concentration of small raindrops with large liquid water content (Petersen et al. 1999; Gochis et al. 2015).

In section 2, we discuss the observational domain, data, and methods used in this analysis, which focuses on measurements from the operational weather radar and soundings at Denver, the Colorado lightning mapping array, two vertically pointing micro rain radars (MRRs), and four surface disdrometers. The spatial and temporal distributions of clouds and precipitation are discussed in section 3. Sections 4 and 5 present the vertical structure of clouds and precipitation along the Front Range (Fig. 1a) as well as near four stations at lower and higher elevations (Fig. 1c). The research is summarized and concluding remarks are provided in section 6. The main objective of this paper is to evaluate the microphysical processes through the spatial distribution of radar variables, rainfall, and vertical profiles of radar reflectivity Z, Doppler velocity, differential reflectivity Z_{dr}, and specific differential phase K_{dp}. While this study focuses on the mesoscale microphysical processes, Friedrich et al. (2015) will discuss the raindrop size distribution observed at the four disdrometer locations.

2. Observational domain, data, and methods

a. Observational domain

The observational domain focuses on the area of intense precipitation during the 2013 Great Colorado Flood, from which unique cloud and precipitation observations were collected. The analysis of cloud and precipitation structures uses observations collected by the National Weather Service Weather Surveillance Radar-1988 Doppler located at Denver, Colorado (location labeled 1 in Fig. 1; WSR-88D Denver, also referred to as KFTG); the operational soundings from Denver; the Colorado lightning mapping array (COLMA); two 24-GHz vertically pointing MRRs, and four Particle Size and Velocity (PARSIVEL) optical disdrometers. Two vertically pointing radars and two disdrometers were deployed around Boulder as shown in Fig. 1c, with one MRR and one disdrometer located on the University of Colorado (CU) campus in Boulder (1663 m MSL; referred to as the CU campus), and one MRR and disdrometer located at the National Center for Atmospheric Research (NCAR) facility at Marshall ~5 km south of the CU campus (1742 m MSL; referred to as Marshall hereafter). Two disdrometers operated by NCAR were also deployed within Fourmile Canyon ~5 km west of the CU campus close to Sugarloaf Mountain (2225 m; referred to as Sugarloaf) and Melvina Hill (2431 m). Rain gauge observations and surface observation stations were also installed at the CU campus, Marshall, and Melvina Hill.

b. WSR-88D Denver radar

Radar reflectivity Z, differential reflectivity Z_{dr}, total differential phase Φ_{dp}, and correlation coefficient ρ_{hv} measurements were provided by the WSR-88D Denver radar (KFTG; 1670 m MSL) every ~4.5 min. NCAR's Radx software[1] was used to calculate the specific differential phase K_{dp} from the Φ_{dp} measured by the radar following Hubbert and Bringi (1995). During the analysis period, the radar scanned with the deep convection configuration (denoted as Volume Coverage Pattern 12

[1] http://www.ral.ucar.edu/projects/titan/docs/radial_formats/radx.html.

or VCP 12) with 14 elevation angles that ranged from 0.5° to 19.5°, with finer elevation angle separation of ~0.5° close to the surface and coarser resolution of up to ~3°–4° at higher-elevation angles. More details about the scan strategy can be found in OFCM (2006). Figure 1 shows the topography around the radar (Fig. 1a), height of the radar beam above ground level for the lowest elevation angle of 0.5°(Fig. 1c), and the fraction of beam blockage at 0.5° (Fig. 1d). The center of the radar beam at the lowest elevation angle of 0.5° is located at 2.2 km MSL (0.6 km AGL; Fig. 1c) at 60-km range, which is approximately the distance between the radar and Boulder (1.6 km MSL). Radar observations at the CU campus and Marshall are not affected by partial beam blockage. Partial beam blockage (<40%) occurs at 0.5° elevation angle at the higher elevation stations at Melvina Hill and Sugarloaf (Figs. 1c,d). Radar data were not adjusted for beam blockage effects. The level-2 radar data were interpolated onto a 0.5 km × 0.5 km × 0.5 km radar grid using the NCAR Radx software package for radial radar data. The vertical spacing (0.5 km) was determined by the tangent of the mean elevation angle close to the surface (0.5°) between two consecutive beams at half distance of the maximum range (60 km). The horizontal spacing (0.5 km) was determined by the range gate spacing of 250 m.

Radar data on the Cartesian grid were used to generate Hovmöller diagrams, contoured frequency by altitude diagrams (CFADs), vertical profiles of median radar quantities, plots of the horizontal distribution of frequency of reflectivity, and hydrometeor classifications using NCAR's particle identification algorithm for S-band radar (also referred to as PID algorithm hereafter; Vivekanandan et al. 1999). The NCAR PID is a fuzzy logic algorithm that uses 14 particle classes to estimate the most dominant contributor to the radar signal in a given range gate. For the Hovmöller diagrams shown in Fig. 2, radar variables were averaged over ~30 km in the north–south direction between the latitude of the surface station located farthest to the south (Marshall) and Longmont (blue box in Fig. 1b). Hovmöller diagrams are shown over 200 km in the east–west direction centered on the radar. Variables shown in the Hovmöller diagrams (e.g., maximum reflectivity and height of the 0-dBZ isoline in Fig. 2) are then derived from the west–east vertical cross section of radar data averaged in the north–south direction.

CFADs, vertical profiles of median Z, Z_{dr}, and K_{dp}, and PID are derived from data observed in a smaller box compared to the Hovmöller diagrams that covers an area of 62 km in the east–west direction and ~30 km in the north–south direction (red box shown in Fig. 1b denoted as CFAD area). The box is centered over the lower foothills extending 38–100 km west of the radar location. The choice of the box size is based on the location of the instruments, the rainfall distribution, and the topography (Fig. 1). CFADs and vertical profiles were derived from each radar volume scan when $Z >$ 0 dBZ and for the two episodes of intense rainfall between 0000 and 0800 UTC 12 September (denoted as first episode) and between 2000 and 0400 UTC 12–13 September (denoted as second episode). The CFADs were normalized by the number of grid cells at each height, as suggested by Yuter and Houze (1995). Median Z, Z_{dr}, and K_{dp} values, together with the 10th and 90th percentiles of these variables, were then derived from the CFADs. In addition to the CFADs showing the vertical profile for the entire episode, median values of Z, Z_{dr}, and K_{dp} from each individual radar scan were derived during the first and second intense rain episodes to study the temporal evolution. To study the temporal evolution of the vertical profiles further and relate it to the surface observations, time series of vertical profiles of radar reflectivity are derived for each instrument site at the CU campus, Marshall, Melvina Hill, and Sugarloaf. Note that in this analysis, radar reflectivity is used as a proxy for rainfall since operational radar-based rainfall estimates show large differences compared to rain gauge observations [see Fig. 11 in Gochis et al. (2015)].

c. COLMA

The COLMA, installed by the New Mexico Institute of Mining and Technology, is a three-dimensional total lightning location system consisting of 15 stations deployed in northeastern Colorado (Wiens et al. 2005; Rison et al. 2012; Lang et al. 2014). The sensors are located between the KFTG radar and the Wyoming border in the north–south direction and between the Front Range and ~60 km east of KFTG in the west–east direction. COLMA measures the time of arrival of lightning discharges at around 60–66 MHz and locates the sources of the radiation to produce a three-dimensional map of total lightning activity (Rison et al. 1999; Krehbiel et al. 2000; Thomas et al. 2001). Three-dimensional total lighting data collected by COLMA was used to study the location and time of individual lightning sources during the intense rain episodes.

d. 24-GHz MRR

The MRR is a vertically pointing Ka-band radar that operates in frequency-modulated, continuous-wave (FM-CW) mode at 24.1 GHz and provides vertical profiles of radar reflectivity and Doppler velocity (Peters et al. 2002). The MRRs deployed at the CU campus and Marshall operated with the same settings and were

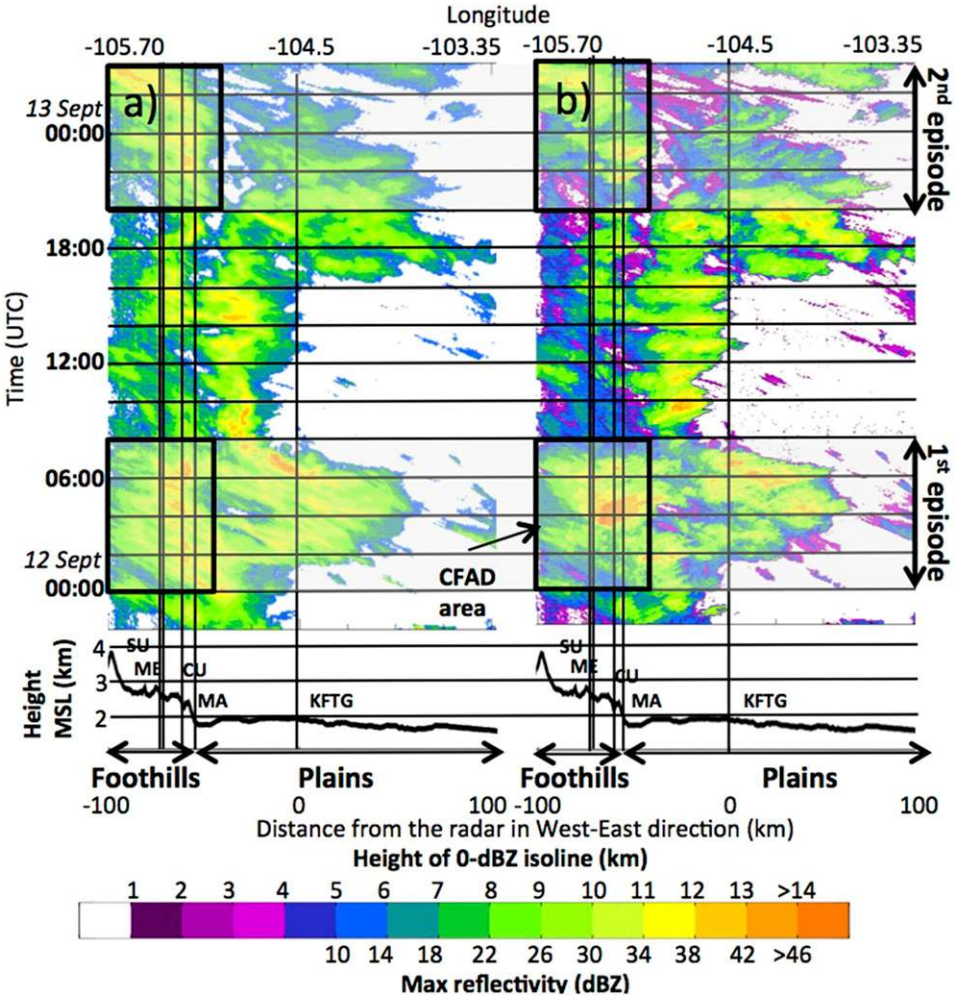

FIG. 2. Hovmöller diagram of (a) maximum reflectivity and (b) height of the 0-dBZ contour for the area shown in the blue box in Fig. 1b. Black lines in the lower panels show mean terrain height profile. Vertical lines indicate the location of the instruments: Sugarloaf (SU), Melvina Hill (ME), CU campus (CU), Marshall (MA), and the KFTG radar; horizontal lines indicate times (upper panels) and heights (lower panels). Black boxes indicate times and areas of CFAD analysis shown in Figs. 11 and 15 (red box in Fig. 1b). Episodes of intense rainfall denoted as first and second episode are shaded in gray.

postprocessed in the same way. The gate spacing was set to 150-m resolution for both instruments. With 30 range gates, measurements were conducted up to a maximum height of 6.16 km MSL at the CU campus and 6.24 km MSL at Marshall. Observations were averaged over 1 min and spurious receiver noise was removed. The MRR Doppler velocity measurement range is 0.95–12.195 m s^{-1}, and the Doppler velocity is the sum of the vertical air motion and the particle fall speed, with positive values representing downward motion. The MRRs have been previously used in various locations to monitor vertical precipitation structures (Löffler-Mang et al. 1999; Peters et al. 2002; Peters et al. 2005; Rollenbeck et al. 2007; Tokay et al. 2009; Trivej and Stevens 2010). Fine temporal and spatial resolution makes the MRR well suited for monitoring changes in the vertical precipitation structure. However, attenuation related to the reflectivity values is expected to be extremely high during the Great Colorado Flood, especially above the melting layer. As such, only the Doppler velocity, which is not affected by attenuation as long as a signal can still be received, will be analyzed in this study.

e. *Surface disdrometers*

In this analysis, four PARSIVEL disdrometers were used to calculate rainfall rates and accumulated rainfall. Note that a more detailed analysis of the drop size distribution is presented in Friedrich et al. (2015). The PARSIVEL disdrometers use a 650-nm laser with a

power of 3 mW (Löffler-Mang and Joss 2000; Löffler-Mang and Blahak 2001). The laser produces a horizontal sheet of light 30 mm wide and 180 mm long, resulting in a horizontal sampling area of 54 cm^2. Particles passing through the horizontal sampling area cause a reduction in the light intensity, which is used to calculate the particle size for particles with diameters between 0.062 and 24.5 mm. A quality-control procedure described in Friedrich et al. (2013a,b) was applied to the data, removing particles classified as margin fallers or splashing and particles misclassified because of strong wind and heavy precipitation effects. Number concentrations were used to calculate rainfall rate R and accumulated rainfall accR.

3. Spatial and temporal distribution of rain

Many places along the Colorado Front Range received rainfall that exceeded the monthly and in some areas the annual average rainfall (Gochis et al. 2015, their Figs. 1a,b). Although rain was observed almost continuously over the 5-day period from 11 to 16 September 2013 over the Colorado Front Range, the heaviest precipitation occurred between 2200 UTC 11 September and 0400 UTC 13 September, when the synoptic and mesoscale patterns favored an upslope easterly flow. The amount and distribution of rain were strongly influenced by the terrain as shown in Figs. 1a and 1b. Continuous intense rainfall was observed in a ~10-km-wide and 50-km-long path between Marshall and Estes Park, with precipitation mainly aligned along the north–south-oriented Front Range centered around the 2-km-MSL contour line (Fig. 1b). Intense rainfall over the foothills (defined as the region higher than 1.6 km MSL) mainly occurred between 0000 and 0800 UTC 12 September and between 2000 and 0400 UTC 12–13 September as shown in the Hovmöller diagrams in Fig. 2a. Note that the Hovmöller diagrams show reflectivity and height of the 0-dBZ radar echo averaged over 30 km in the north–south direction along a 200-km-wide west–east transect centered at the radar (Fig. 1b, section 2a). In addition to the intense rainfall over the foothills, intense rainfall also occurred 10–20 km farther downstream over the plains (≤1.6 km MSL) along a north–south-oriented path that stretched from southeast of Longmont to southwest of Denver (Fig. 1b) mainly during 0000–2000 UTC 12 September (Fig. 2a). Since no surface observations were available in the downstream area, the analysis solely focuses on rainfall over the foothills (red box in Fig. 1b and black boxes in Fig. 2 denoted as CFAD area). Note that severe radar beam blockage (>80%) occurred beyond 2.5 km MSL, causing a sudden decrease in reflectivity farther away from the radar over the higher terrain (cf. Figs. 1b, d and 2).

Large spatial variations in rainfall were observed even within the swath of heavy rainfall, as indicated by four disdrometers located within the lower terrain at Boulder and Marshall (~1.6–1.7 km MSL) and the higher terrain at Melvina Hill and Sugarloaf (2.2–2.4 km MSL). Accumulated rainfall and rainfall rates at the four stations (Figs. 3a,b) and surface observations at Marshall are shown in Figs. 3c and 3d. The CU campus, located within the area of maximum rainfall, received ~230 mm of accumulated rainfall over 30 h between 11 and 13 September, while Marshall, located at the edge of the intense precipitation region, observed 190 mm during the same time period. The mountain station Sugarloaf received about 110 mm. The disdrometer at Melvina Hill did not operate between 0900 and 1645 UTC, 1900 and 2045 UTC, and after 2315 UTC 12 September. The accumulated rainfall at Melvina Hill during the time it operated was 110 mm. As shown in Fig. 3, intense rainfall occurred during two episodes when easterly winds favored orographic enhancement 1) between 0000 and 0800 UTC 12 September with rainfall rates of up to 70 mm h^{-1} at the CU campus (referred to as the first episode hereafter) and 2) between 2000 and 0400 UTC 12–13 September with rainfall rates of up to 60 mm h^{-1} at the CU campus (referred to as the second episode hereafter). These time periods of intense rainfall will be analyzed hereafter.

During the first episode, widespread precipitation with embedded convective cells occurred from the lower up to the higher terrain as shown in the Hovmöller diagram in Fig. 2a, the frequency analysis (Fig. 4a), and individual horizontal cross sections of radar reflectivity (Fig. 5). Over the foothills between Marshall and Estes Park, reflectivity values were >30 dBZ over 65% of the time, as shown in the frequency analysis in Fig. 4a. At the same time, an east–west-oriented band of high frequency (>40% with $Z > 30$ dBZ) was observed along the northern side of the Palmer Divide east of Boulder (Fig. 4a). Radar reflectivity at 3 km MSL (Fig. 5) reveals that rain occurred over almost the entire episode, with enhanced convection over the foothills. In addition, a distinct, narrow, east–west-oriented line of enhanced reflectivity developed over the plains at around 0130 UTC, widened with time, and remained present through the rest of the episode (Fig. 5). Although the distribution of intense rainfall followed the rising topography along the Front Range and Palmer Divide, the rainfall intensity was also strongly linked to low-level convergence (Friedrich et al. 2015). Persistent easterly low-level flow triggered intense precipitation over the foothills (Figs. 3, 5). In addition, mesoscale surface

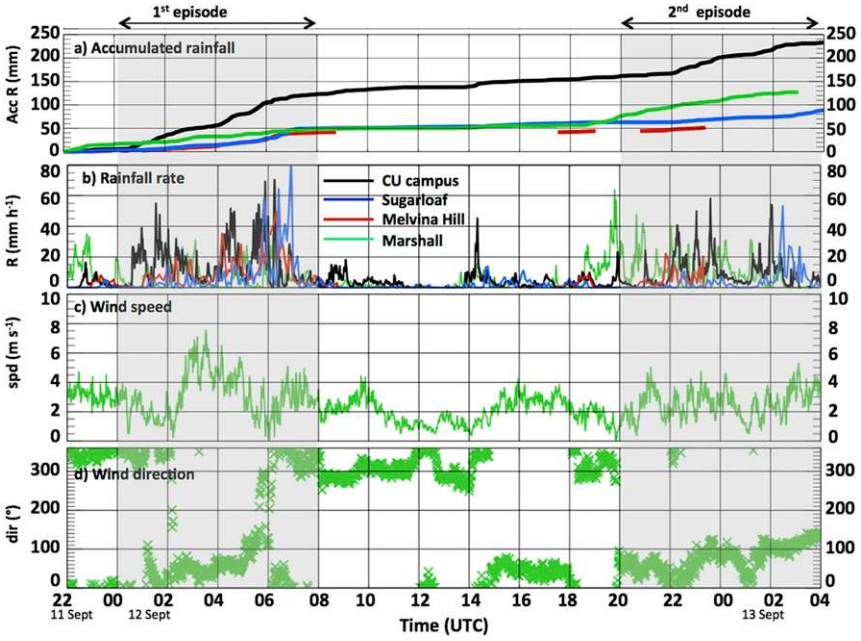

FIG. 3. Surface observations between 2200 and 0400 UTC 11–13 Sep: (a) accumulated rainfall and (b) rainfall rate observed based on surface disdrometers at CU campus (black lines), Marshall (green lines), Sugarloaf (blue lines), and Melvina Hill (red lines). (c) Wind speed and (d) direction observed at Marshall. First and second episodes of intense rainfall are highlighted with gray shading. In (a) and (b), the disdrometer at Melvina Hill did not operate between 0900 and 1645 UTC, 1900 and 2045 UTC, and after 2315 UTC 12 Sep.

features most likely enhanced convection over the plains and foothills. One of these mesoscale features is a cyclonic circulation indicated by the Variational Doppler Radar Analysis System (VDRAS; Sun and Crook 1997; Gochis et al. 2015, electronic supplement A; Friedrich et al. 2015). Note that this feature does not appear as a closed circulation at the surface but radar observations, VDRAS, and numerical simulations

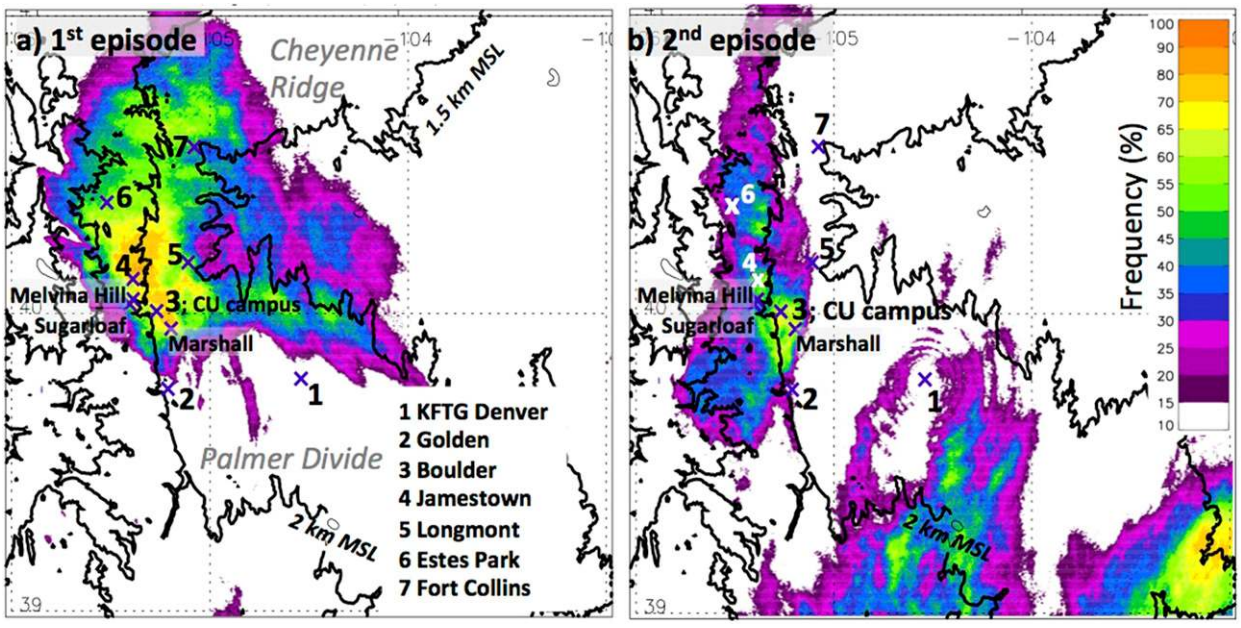

FIG. 4. As in Fig. 1b, but showing frequency of $Z > 30$ dBZ occurring during the (a) first and (b) second episodes.

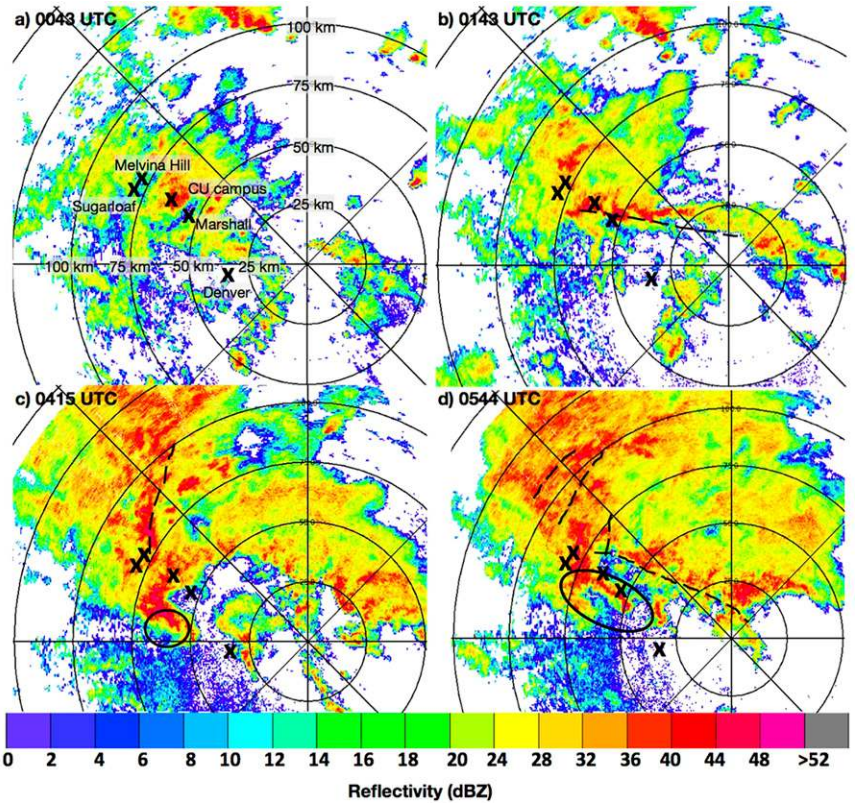

FIG. 5. Horizontal distribution of reflectivity at 3 km MSL observed by the KFTG radar at Denver at (a) 0043, (b) 0143, (c) 0415, and (d) 0544 UTC 12 Sep. Dashed black lines indicate the location of the convergences (cf. Fig. 6). The mesoscale circulation discussed in section 4a is indicated by a black circle in (c) and the black oval in (d) (cf. Figs. 6c,d).

indicate a circulation at 1–2 km AGL. Doppler velocity fields at 3 km MSL first indicate the circulation over the city of Denver at 0143 UTC (southernmost cross sign in Fig. 6b). It moved into the Boulder area at 0300 UTC, enhancing convection over the Front Range (circulation indicated in Figs. 5c,d and 6c,d). A second east–west-oriented line of enhanced low-level convergence in wind speed, indicated as an increase in Doppler velocity in Fig. 6b, occurred just north of the radar along the northern side of the Palmer Divide east of Boulder. An east–west-oriented line of enhanced reflectivity observed at ~0200 UTC (Fig. 5b) was associated with this convergence. Several convergence zones were observed over the foothills after 0430 UTC (dashed lines in Figs. 6c,d; Friedrich et al. 2015). As a result, convergence associated with the mesoscale circulation and later with the converging boundaries dominated the evolution and enhancement of precipitation over the plains and foothills.

During the first episode (1800–0000 LT 11 September; 0000–0800 UTC 12 September), the CU campus received 110 mm of rainfall over 8 h (Fig. 3a). While rainfall rates greater than 20 mm h^{-1} were observed during the middle of the first episode (0000–0300 UTC) because of steady easterly flow, precipitation significantly increased after 0400 UTC, likely due to the converging boundaries of the mesoscale circulation, that is, a region of cyclonic horizontal shear and convergence, centered around Boulder (Figs. 5c, 6c). Surface temperature at Marshall was steady at ~15°C (not shown) and surface wind speeds were less than 8 m s^{-1} (Fig. 3c). The Marshall site, located only ~5 km southeast of Boulder, observed much lower rainfall rates and accumulated rainfall ($R < 30$ mm h^{-1}; accR = 60 mm) during most of the first episode. Rainfall rates at Marshall increased only occasionally up to 30 mm h^{-1} after 0200 UTC and from 0430 to 0600 UTC, associated with the lines of enhanced reflectivity and convergence passing over Marshall (Figs. 5c,d and 6c,d). Even smaller rainfall rates ($R < 20$ mm h^{-1}) relative to the CU campus and Marshall were observed at the mountain stations at Sugarloaf and Melvina Hill. The convergence zone shown in Fig. 6d moved farther into the foothills, reaching Sugarloaf and Melvina Hill at around

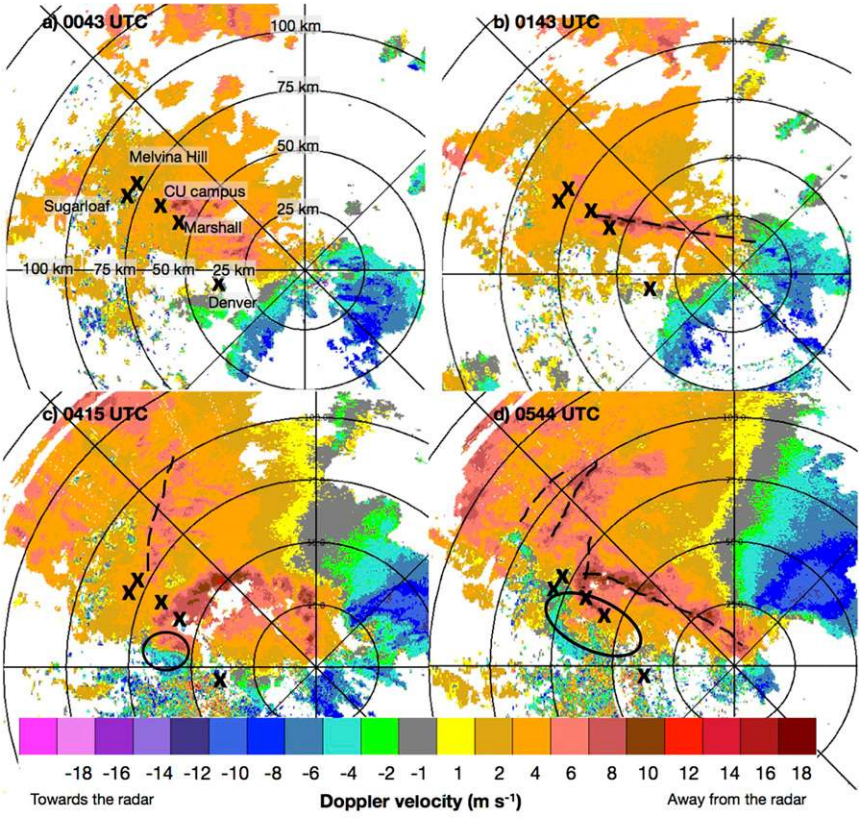

FIG. 6. As in Fig. 5, but for Doppler velocity.

0600 UTC, resulting in an increase in rainfall rate up to 70–80 mm h^{-1} at Sugarloaf and 50 mm h^{-1} at Melvina Hill. It would be worthwhile to investigate how the convergence zones interacted with the topography to affect surface precipitation, but this subject is beyond the scope of this paper. In addition to the low-level convergence zones, easterly upslope flow and a moist neutral-to-unstable atmosphere might have favored orographic enhancement of precipitation.

The second episode of heavy rainfall occurred between midafternoon and late evening (1400–2200 LT; 2000–0400 UTC). Rain was mainly located over the foothills around the 2-km-MSL contour at Boulder and south of Boulder (Fig. 4b). The Hovmöller diagram shows that intense rain occurred between Marshall and Melvina Hill with weak rain over the plains (Fig. 2a). Although reflectivity values >30 dBZ were observed, they occurred less frequently (<60% of the time) compared to the first episode (Fig. 4b). At the CU campus (Marshall), the accumulated rainfall (~70 mm both at the CU campus and Marshall) was lower (slightly higher) during the second episode compared to the first episode (Fig. 3). Lower accumulated rainfall was also observed at the higher-elevation stations during the second compared to the first episode (~35 mm at Sugarloaf). The surface temperature at Marshall was around 15°C with weaker easterly winds compared to the first episode of 6 m s^{-1} (Fig. 3c). Radar reflectivity at 3 km MSL observed during the second episode as shown in Fig. 7 reveals that large reflectivity values (up to 50 dBZ) were first observed close to Boulder and southeast of Denver between 2000 and 0000 UTC (Fig. 7a). After 0000 UTC, precipitation and reflectivity weakened over the plains and intensified over the foothills (Figs. 7b,d). Large spatial variations in rainfall were still apparent (Figs. 3a, 7). Doppler velocity fields at 3 km MSL shown in Fig. 8 indicate steady easterly surface flow with Doppler velocity values of ~10 m s^{-1}. This low-level wind maximum peaking at 2.5 km MSL was also observed by the operational sounding at Denver over the entire episode (Fig. 9b). Contrary to the surface observations at Marshall, which showed a decrease in wind speed with time (Fig. 3c), the magnitude of the low-level wind maximum at 2.5 km MSL as observed by the Denver sounding increased from 10 to 13 m s^{-1} between the first and second episode (Fig. 9b).

Over the entire event, most of the intense and persistent rainfall occurred around Boulder and within a 10-km swath between Boulder and Estes Park (Fig. 1b). Although the operational Z–R relationship failed to

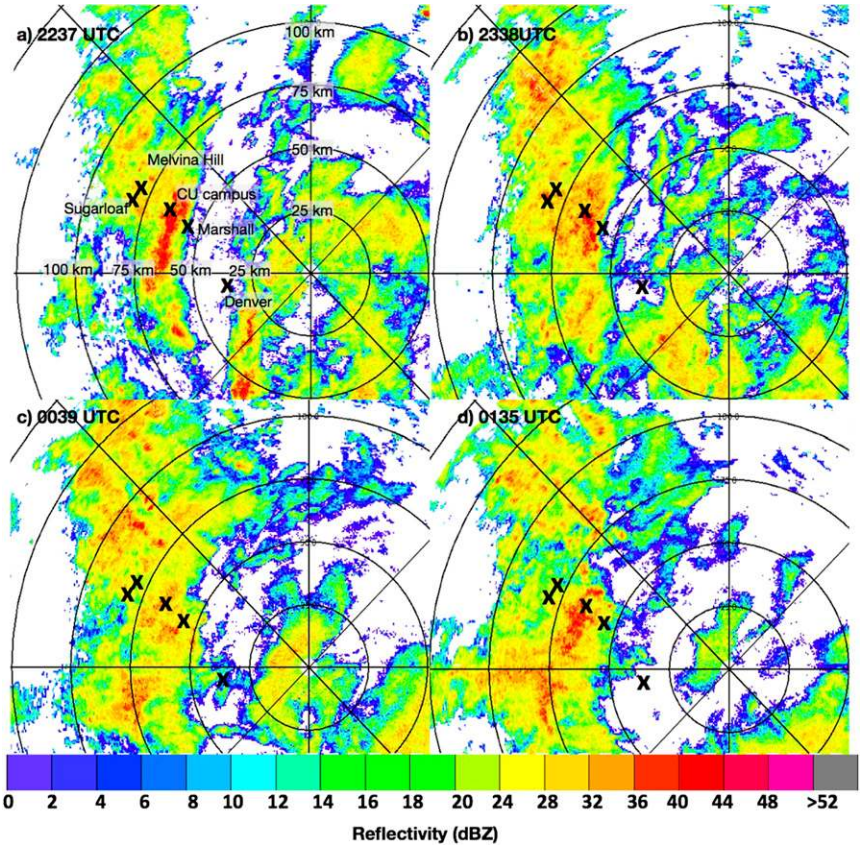

FIG. 7. As in Fig. 5, but for the second episode at (a) 2237 and (b) 2338 UTC 12 Sep and (c) 0039 and (d) 0135 UTC 13 Sep.

reproduce the amount of rainfall (Gochis et al. 2015), a frequency analysis of radar reflectivity as shown in Fig. 4 already revealed that certain communities and watersheds received above-average rainfall. Figure 4a showed that during the first episode, Boulder and areas northwest of Boulder continuously received intense rainfall over many hours, which continued throughout the second episode.

4. Vertical structure of clouds and precipitation over the foothills

a. Vertical structure of the atmosphere

The operational sounding at Denver (0000 UTC 12 and 13 September; Fig. 9) indicated that the atmosphere was saturated up to ~5 km MSL with slightly decreasing moisture at 0000 UTC 13 September (Fig. 9a). The 0°C level was located at 4.8 km MSL at the beginning of the first episode, decreasing slightly to 4.4 km during the second episode (Fig. 9a). The mixing ratio ranged between 5 and 12 g kg^{-1} below the freezing level (Fig. 9a). A shallow layer of absolutely unstable air ($\delta\theta_e/\delta z < 0$) was observed from close to the surface up to 2.5–3 km MSL during the entire event and at 5.5–7 km on 12 September and 4–6 km on 13 September (Fig. 9c). Cross-barrier easterly surface winds were only observed up to 3 km (4 km) MSL at 0000 UTC 12 September (13 September; Fig. 9b). A low-level wind maximum with speeds of 8–13 m s^{-1}, oriented perpendicular to the terrain (dashed lines in Fig. 9b), was present at ~2.5 km MSL. Above the 0°C level, westerly to southwesterly winds were observed (not shown). Note that 24 h prior to the intense rain episodes, clouds with mean infrared brightness temperatures ranging from −10° to −30°C and light rainfall with maximum rates of 5 mm h^{-1} were observed almost continuously [Fig. 8 in Gochis et al. (2015)]. As a result, the lack of sun weakened the instability, favoring weak convection.

b. Z, Z_{dr}, and K_{dp} profiles during the first episode

During the first episode, clouds and precipitation were observed over both the plains (elevation ≤ 1.6 km MSL) and foothills (elevation > 1.6 km MSL), as shown in Fig. 10. At the beginning of the first episode (0000–0300 UTC), taller and more vigorous clouds first developed

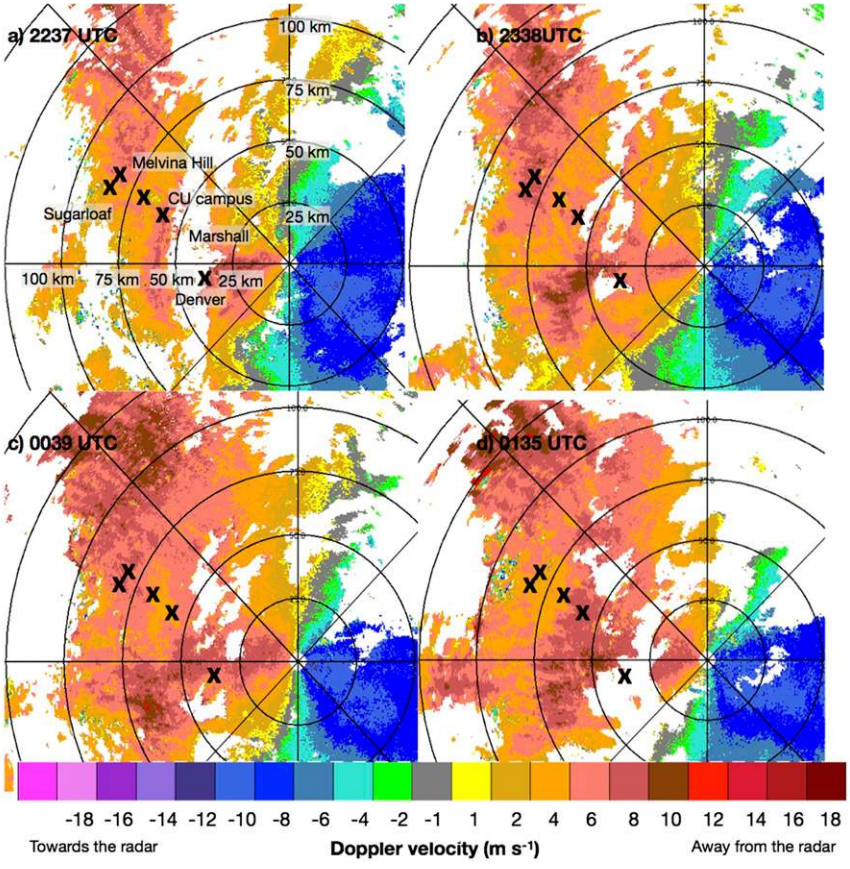

FIG. 8. As in Fig. 7, but for Doppler velocity.

over the plains when surface convergence zones related to the mesoscale circulation approached the investigation area. Radar returns over the foothills were shallower (<6 km MSL). With time (0300–0700 UTC), radar returns over the foothills became taller and reflectivity values increased (Figs. 2 and 10d–g). The largest vertical extent in reflectivity was observed at the lower foothills right at the transition between the foothills and plains. During that time (0400–0500 UTC), the mesoscale circulation associated with multiple convergence lines moved into the area (section 3). As such, the vertical extent of radar returns increased significantly after 0300 UTC (Figs. 2b, 10). While occasionally a melting layer at 4.5–5 km MSL associated with a strong increase in reflectivity with decreasing height can be observed in Fig. 10, convective cells embedded in the stratiform rain dominated the first episode.

To further study microphysical processes, CFADs over the entire episode and vertical profiles of median Z, Z_{dr}, and K_{dp} for each radar scan shown in Fig. 11 were calculated (section 2b). CFADs and vertical profiles were derived over an area of 62 km in the west–east direction and 30 km in the north–south direction west of the radar over the foothills (domain is indicated in Figs. 1b, 2). Particles with small median reflectivity of ~10 dBZ, small median Z_{dr} values of ~0.2 dB, and maximum median K_{dp} values around 0.15° km^{-1} were observed at higher levels (>6.5 km MSL with $T < -10$°C; Fig. 11). Areas of positive K_{dp} (~0.2°–0.6° km^{-1}) and positive Z_{dr} (~0.3–0.4 dB) near the −15°C level have been associated with active dendritic particle growth (e.g., Ryzhkov et al. 1998; Trapp et al. 2001; Andric et al. 2010; Kennedy and Rutledge 2011). Kennedy and Rutledge (2011) showed that continuous upward air motion provided a water-saturated environment in order to grow dendritic particles rapidly with diameters of 0.8–1.2 mm and bulk density >0.3 g cm^{-3}. During the first episode, enhanced K_{dp} values (>0.15° km^{-1}) were primarily observed during 0300–0500 UTC (turquoise, green, and yellow lines in Fig. 11f), while K_{dp} was slightly lower prior to 0300 UTC and after 0500 UTC. Irregular ice crystals and dry snow were classified as the dominant particles based on the dual-polarization values (Fig. 12a). At about 6 km MSL, Z_{dr} decreased to 0 dBZ, indicating more spherical particles. Enhanced cloud supercooled liquid (>0.4 g m^{-3}) was

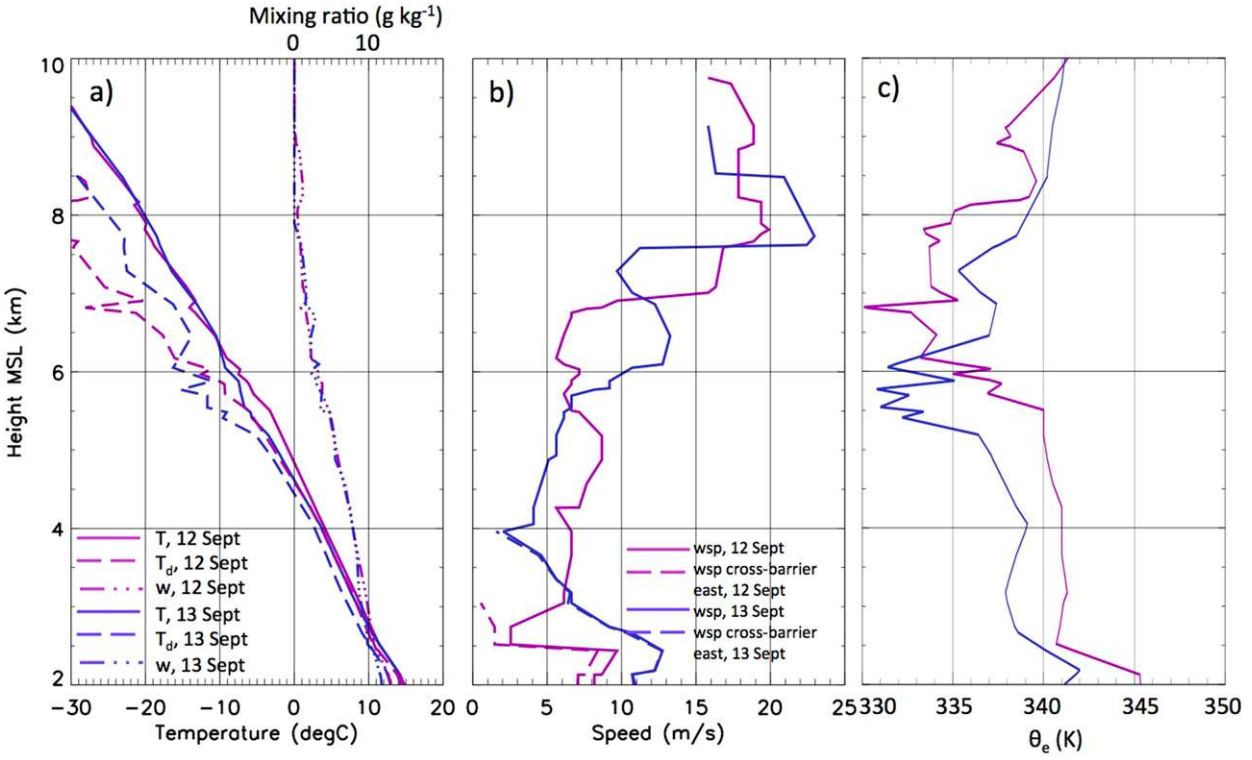

FIG. 9. Vertical profiles of (a) temperature T (solid line) and T_d (dashed line) and mixing ratio w (dashed–dotted line), (b) wind speed (solid line) and cross-barrier wind speed (dashed line), and (c) equivalent potential temperature θ_e based on operational Denver soundings at 0000 UTC 12 Sep (magenta lines) and 13 Sep (blue lines). Cross-barrier easterly wind speed in (b) was only observed up to 3 km on 12 Sep and 4 km on 13 Sep; wind veered to westerly above these heights.

observed by a microwave radiometer located in Boulder between 0230 and 0400 UTC at 6–7 km MSL (figure not shown). The presence of supercooled liquid indicating enhanced riming and graupel production is further supported by the occurrence of lightning above 5 km MSL observed between 0330 and 0430 UTC shortly after the enhanced supercooled liquid was observed by the radiometer (Fig. 13). Lightning activity mainly occurred over the foothills between Marshall and Sugarloaf (0330–0500 UTC) and moved northward after 0530 UTC. A steady updraft, either orographically forced or through convection, is usually sufficient to maintain liquid water drops above the 0°C level in the presence of falling ice particles, favoring riming (e.g., Rauber et al. 1986; Rauber and Grant 1986, 1987; Marwitz 1987; Heggli and Rauber 1988; Ikeda et al. 2007). The PID algorithm identified both dry and wet snow between 5 and 7 km MSL (Fig. 12a), which indicates that aggregation might have occurred at times. In particular, between 6 and 7 km, mean Z and Z_{dr} profiles increase and decrease with decreasing height, respectively, as is typically observed during aggregation (Ryzhkov et al. 1998). Although the small mean drop sizes at the surface do not support aggregation being dominant during the entire episode, large concentrations of medium-sized drops with $d \sim 2$–4 mm were observed occasionally during the short times of intense precipitation with $R > 20\,\text{mm}\,\text{h}^{-1}$ (Fig. 3b). The Z and Z_{dr} increase rapidly with decreasing height between 5 and 6 km, indicating rapid growth of particles primarily through riming and/or aggregation.

A sudden increase in Z with decreasing height to ~30 dBZ and a peak in Z_{dr} were observed by the KFTG radar between ~4 and 5 km MSL close to the 0°C level (Fig. 11). Melting layer characteristics typical for stratiform precipitation, such as the sharp decrease in Z with decreasing height usually observed below the 0°C level due to large ice particles melting into generally smaller raindrops ($Z \sim d^6$) and the increase in fall velocity generating a downward flux of precipitation mass, were not present during the entire first episode. It supports the convective nature of the precipitation during the first episode. Note that the melting layer is usually located within a 0.5-km-thick layer below the 0°C level, which is at ~4.5–5 km MSL (Houze 1993). Below 4 km MSL, the width of the frequency diagrams increased because of the cumulative effects of evaporation, raindrop breakup, and collision–coalescence (Fig. 11a). Median Z

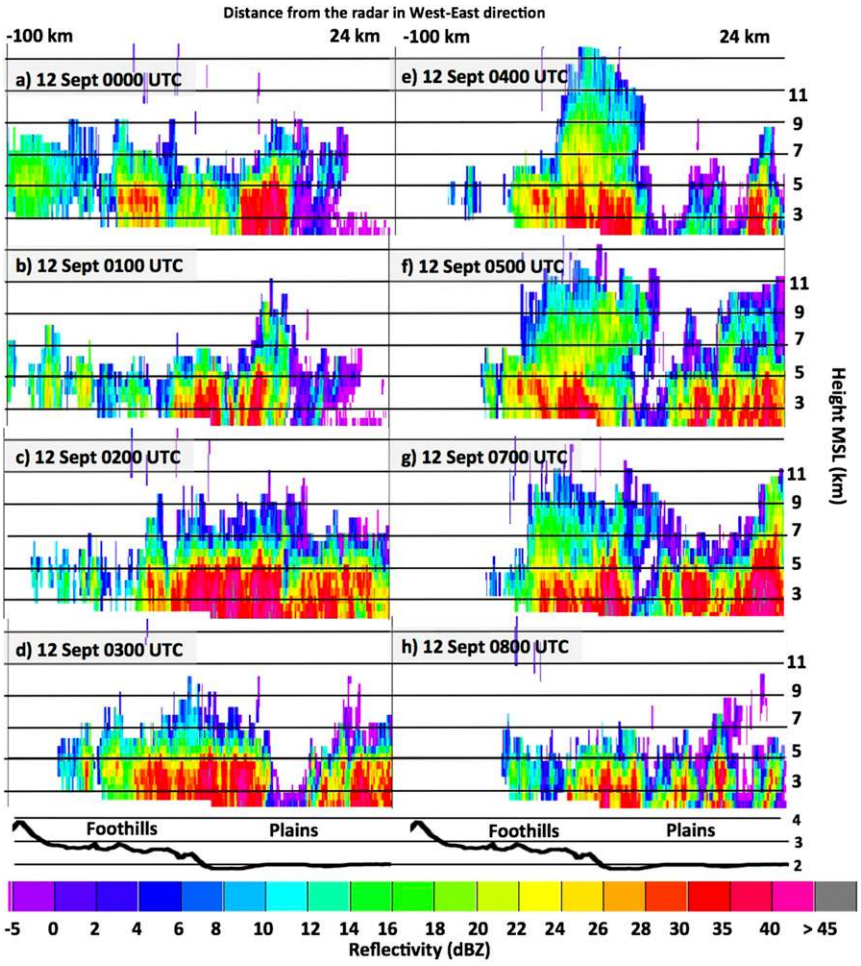

FIG. 10. Vertical cross sections of radar reflectivity during the first episode. Cross sections were generated at the latitude of Boulder using the KFTG radar reflectivity. The topography is indicated at the bottom with a separation of the foothills with heights > 1.6 km MSL and the plains with heights ≤ 1.6 km MSL.

and Z_{dr} profiles remained constant with decreasing height (Figs. 11a,b). The median reflectivity values for each time step varied greatly with time (Fig. 11d). Nearly constant Z was observed between 0000 and 0300 UTC, indicating a balance among collision–coalescence, evaporation, and raindrop breakup. In contrast, a decrease in Z with decreasing height was observed between 0300 and 0500 UTC, indicative of raindrop demise either through breakup or evaporation. Last, an increase in Z with decreasing height was observed after 0600 UTC, indicating growth through collision–coalescence. Note that the probability of raindrops with $d \sim 1.0$–1.5 mm breaking up is nearly zero based on the empirical formula of Srivastava (1971). While the mean raindrop diameter was around 1 mm, larger raindrops ($d > 2$ mm) were occasionally observed [Fig. 2 in Friedrich et al. (2015)]. Particles below the 0°C level classified by the PID algorithm were mainly light to moderate precipitation with a few instances of small hail, graupel, and wet snow (Fig. 12a). Note that graupel and hail were not observed at any of the disdrometer locations. The small particle diameter is reflected in light and moderate rain classified by the PID.

c. Z, Z_{dr}, and K_{dp} profiles during the second episode

During the second episode, intense persistent rain mainly occurred over the foothills above 1.6 km MSL with a few intense rain showers over the plains at and below 1.6 km MSL (Figs. 3a, 4b, 7). No lightning activity was observed by the COLMA between 2000 UTC 12 September and 0200 UTC 13 September. Note that no lightning data were available between 0200 and 0400 UTC 13 September. Figure 14 presents vertical cross sections of reflectivity for selected times during the second episode. At the beginning of the second episode (2000–0000 UTC), radar returns were shallow but

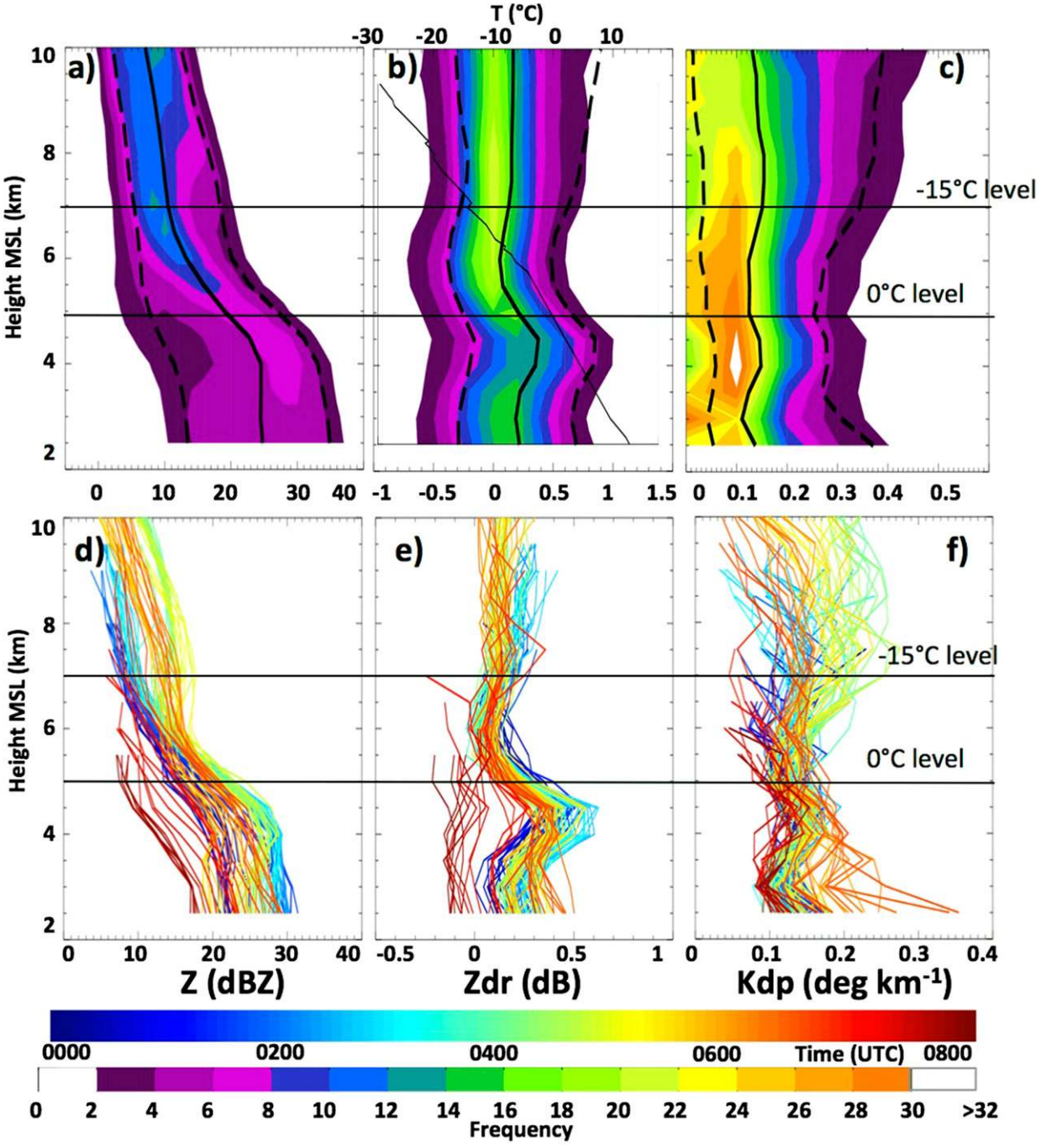

FIG. 11. (top) CFADs and (bottom) median vertical profiles at each radar scan of (a),(d) Z; (b),(e) Z_{dr}; and (c),(f) K_{dp} during the first episode between 0000 and 0800 UTC 12 Sep. CFADs and profiles were computed over the domain displayed in Fig. 1b (red box denoted as CFAD area) and Fig. 2 (black box). Shown in (a)–(c) is frequency distribution as a function of height over the entire first episode normalized by the number of pixels at each height (bottom color bar). Median values over the first episode (black solid line) and 10th and 90th percentiles (dashed lines) are highlighted. Shown in (d)–(f) is median values for each radar scan with colors corresponding to times (upper color bar). Solid black line in (b) indicates the temperature profiles based on the Denver sounding at 0000 UTC 12 Sep. Horizontal black lines highlight the 0°, −15°, and −15°C levels, respectively.

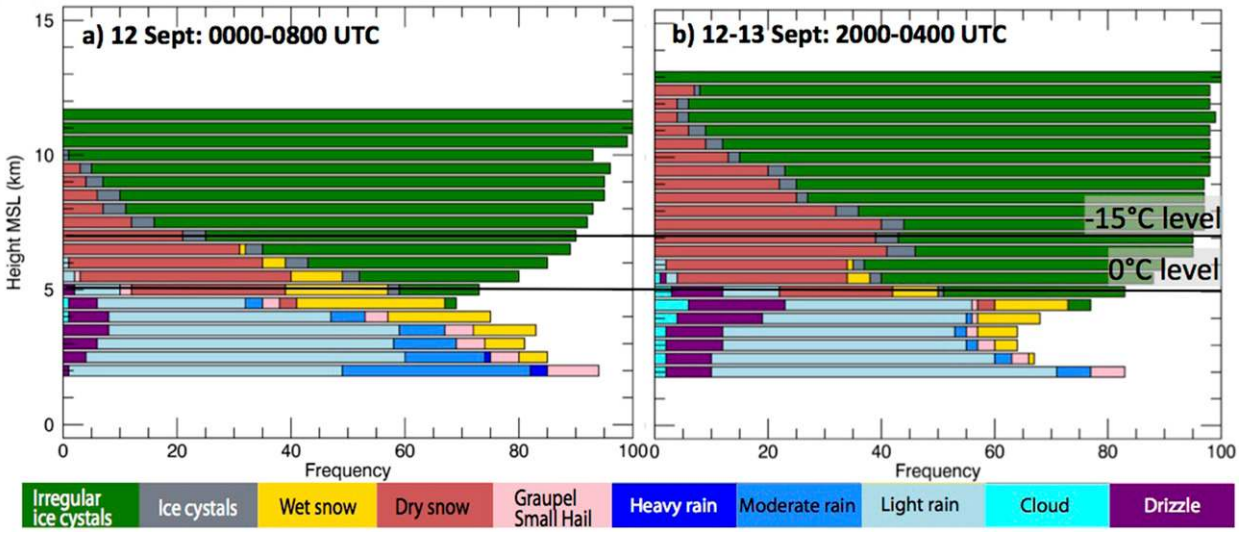

FIG. 12. Normalized frequency of occurrence of hydrometeor classification by height (km) for the time period (a) 0000–0800 UTC and (b) 2000–0400 UTC using KFTG radar data. Horizontal black lines indicate the 0° and −15°C levels. The frequency analysis is computed over the domain displayed in Fig. 1b (red box denoted as CFAD area) and Fig. 2 (black box).

occasionally showed an increase in Z below the 0°C level (Figs. 14a–d). After 0200 UTC, the vertical extent of the radar returns exceeded 11 km MSL and large reflectivity values at the surface were observed over the foothills almost continuously (Figs. 14f–h). A melting layer, indicated by an increase and decrease in radar reflectivity with decreasing height around the 0°C level, can be identified more clearly and frequently during the second compared to the first episode, suggesting more stratiform precipitation in particular toward the end of the episode (Fig. 14g). Nevertheless, convective precipitation, in particular at the beginning of the second episode, was still observed.

Figure 15 presents the frequency and median values of Z, Z_{dr}, and K_{dp} as a function of height. Median reflectivity at the surface was lower during the second episode compared to the first episode (25 dBZ versus 21 dBZ; Figs. 11a, 15a), and the median profiles for the individual times show greater temporal variability (Figs. 11d, 15d). Above 6 km MSL, Z increases rapidly with decreasing height, while Z_{dr} and K_{dp} show enhanced maxima between 6 and 8 km MSL. In particular, a large increase in Z was observed after 0200 UTC close to the −15°C level, which was accompanied by an increase in Z_{dr} and K_{dp}. Clouds grew taller after 0200 UTC (Figs. 14e–h), reaching areas with $T < -15$°C. The increase in Z, Z_{dr}, and K_{dp} might be an indication of rapid growth of dendritic particles. Interestingly, the increases are more pronounced during the second episode compared to the first episode (cf. Figs. 11a–c, 15a–c). Reflectivity continued to increase with decreasing height, while Z_{dr} and K_{dp} rapidly decreased with decreasing height between 5 and 6 km, which is most likely an indication of aggregation (Ryzhkov et al. 1998). Supercooled liquid was only observed occasionally by the microwave radiometer between 2000 and 2359 UTC 12 September (figure not shown). Contrary to the first episode, aggregation might have been more dominant during the second episode. Below the melting layer (<4 km MSL), large variations in Z and Z_{dr} were observed. During the earlier times (2000–0100 UTC; blue to green to yellow lines in Fig. 15d), reflectivity increased with decreasing height and remained constant later on. Later on (after 0200 UTC), reflectivity slightly decreased with decreasing height, indicating raindrop decay either through raindrop breakup or evaporation. Similar to the first episode, the overall median Z and Z_{dr} profiles remained constant between the melting layer and the surface (Figs. 15a,b). Compared to the first episode, liquid water and wet snow were observed at fewer times above the 0°C layer during the second episode (Fig. 12b). Surface disdrometers at the CU campus and Marshall occasionally observed large rainfall rates and small drop sizes during the second episode. The latter resulted in low radar reflectivity and precipitation classified by the radar as light rain and drizzle.

d. Comparison to monsoon–ocean and tropical convection and orographic rainfall

The Denver sounding already indicated the tropical nature of the atmosphere during the Great Colorado Flood with high precipitable water, moist conditions throughout the troposphere, relatively small convective

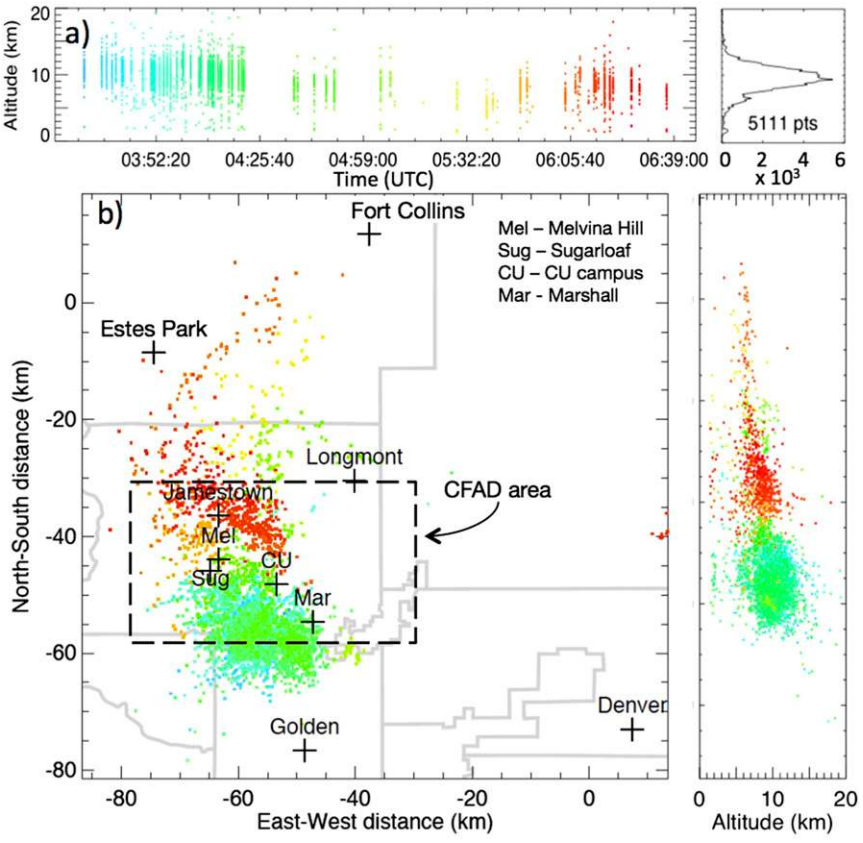

FIG. 13. Lightning sourced from the COLMA between 0320 and 0650 UTC 12 Sep 2013: (a) time–height plot showing the vertical location as a function of time indicated by color. Total lightning sources as a function of height is shown in the right panel with the maximum number indicated. (b) Horizontal distribution of lightning with longitudinal height plot in the right panel. The black box indicates the CFAD area shown in Figs. 11 and 15. Gray lines indicate county borders.

available potential energy (CAPE), and low cloud base with a high 0°C level (Gochis et al. 2015; section 4a). The Denver sounding during the Great Colorado Flood resembled those observed during the Tropical Ocean and Global Atmosphere Coupled Ocean–Atmosphere Response Experiment (TOGA COARE; Webster and Lukas 1992), the Global Atmospheric Research Program (GARP) Atlantic Tropical Experiment (GATE; International and Scientific Management Group for GATE 1974), and the 1997 Fort Collins flash flood (FCL; Petersen et al. 1999). While the atmosphere during the Great Colorado Flood showed characteristics of a tropical environment, the following section discusses if the vertical cloud structure and microphysical processes resemble those observed in monsoon–ocean and tropical environments and orographic rainfall in coastal regions. One common feature observed in tropical convection is the rapid decrease in reflectivity above the 0°C level and low reflectivity throughout the upper troposphere (Williams et al. 1992; Rutledge et al. 1992; Zipser and Lutz 1994). Figure 16 shows the mean reflectivity normalized by the maximum value during the first and second intense rain episodes during the Great Colorado Flood compared to normalized reflectivity profiles from TOGA COARE, GATE, and FCL. Note that the vertical structure of reflectivity during the 1997 Fort Collins flood, trigged solely through upslope flow along the foothills, showed some resemblance to that observed in tropical monsoon–ocean convection. While the depth of the coalescence layer (layer between cloud base and 0°C level) is much deeper during the tropical convection, the sharp increase in reflectivity with decreasing height during the Colorado Flood is similar to those in tropical and monsoon convection. Zipser and Lutz (1994) compared reflectivity lapse rates between 0° and −20°C as a function of maximum reflectivity (their Fig. 5). The maximum reflectivity of tropical convection ranged

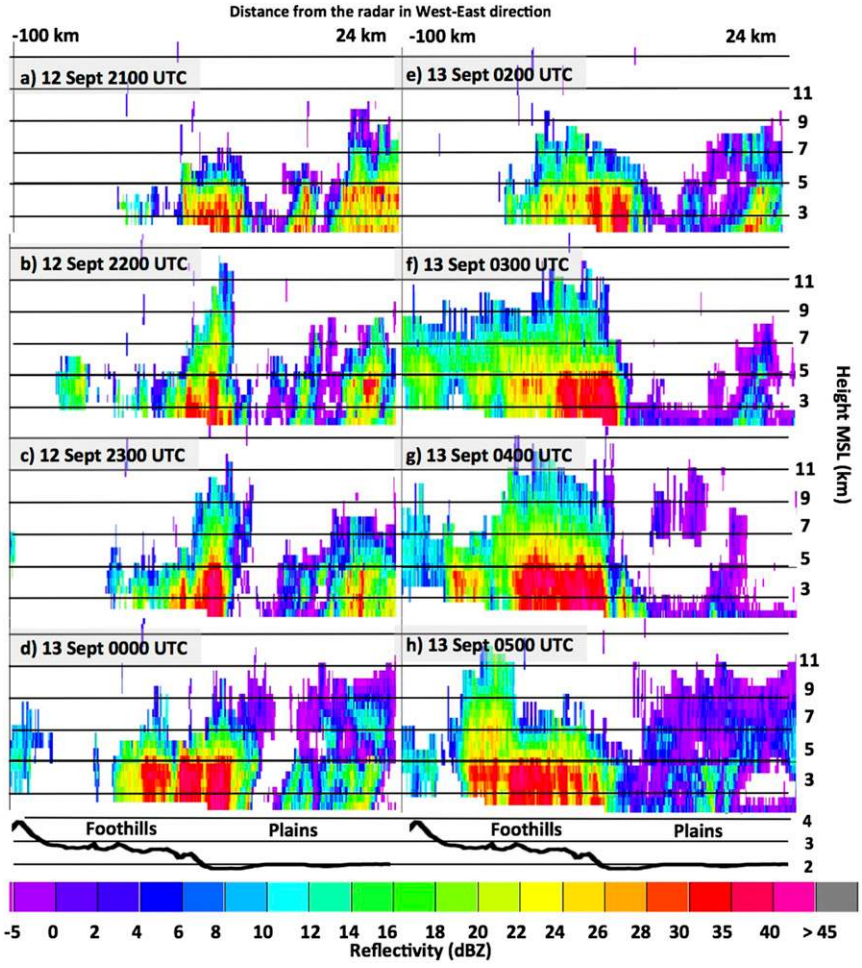

FIG. 14. As in Fig. 10, but for the second episode between 2100 and 0500 UTC 12–13 Sep.

between 32 and 44 dBZ (compared to 42–54 dBZ in midlatitude convection) and the reflectivity lapse rates ranged from 10 to 25 dBZ (compared to a range from −1 to 15 dBZ in midlatitude convection). During the Great Colorado Flood, the mean maximum reflectivity was about 35 dBZ (32 dBZ) with a lapse rate between 0° and −20°C of 15 dBZ (20 dBZ) during the first (second) intense rain episodes (figure not shown). Another similarity between tropical convection and the Great Colorado Flood is that, in both cases, large radar reflectivity values ($Z > 35$ dBZ) were generally observed near or below the −10°C level. A similar behavior in the vertical profile of reflectivity can also be observed in nonbrightband orographic rain in the coastal mountains of California (White et al. 2003). During their nonbrightband cases, maximum reflectivity peaks at 19 dBZ close to the surface, reflectivity lapse rates are about 25 dBZ over 1 km, and the maximum reflectivity occurs below the average brightband height [Fig. 13 in White et al. (2003)]. White et al. (2003) concluded for their cases that both the low-level reflectivity maxima and the high reflectivity lapse rates are an indication of the dominance of warm rain processes.

In addition, thunderstorm electrification can be used to quantify ice–ice collision processes, which require the presence of supercooled liquid water. Little lightning activity has been observed in monsoon and tropical ocean regimes (Orville and Henderson 1986; Goodman and Christian 1993; Zipser 1994), while continental storms often exhibit very high lightning flash rates. Wiens et al. (2005) showed that a supercell thunderstorm in northeastern Colorado had lightning flash rates of nearly 300 per minute. They further state that the lightning mapping array locates from hundreds to thousands of VHF sources for a given lightning flash. During the Great Colorado Flood, the maximum value of VHF sources only reached 5111 over 3 h during the first intense episode (Fig. 13a), which is relatively low for convective storms in Colorado. During the second episode, no lightning was observed.

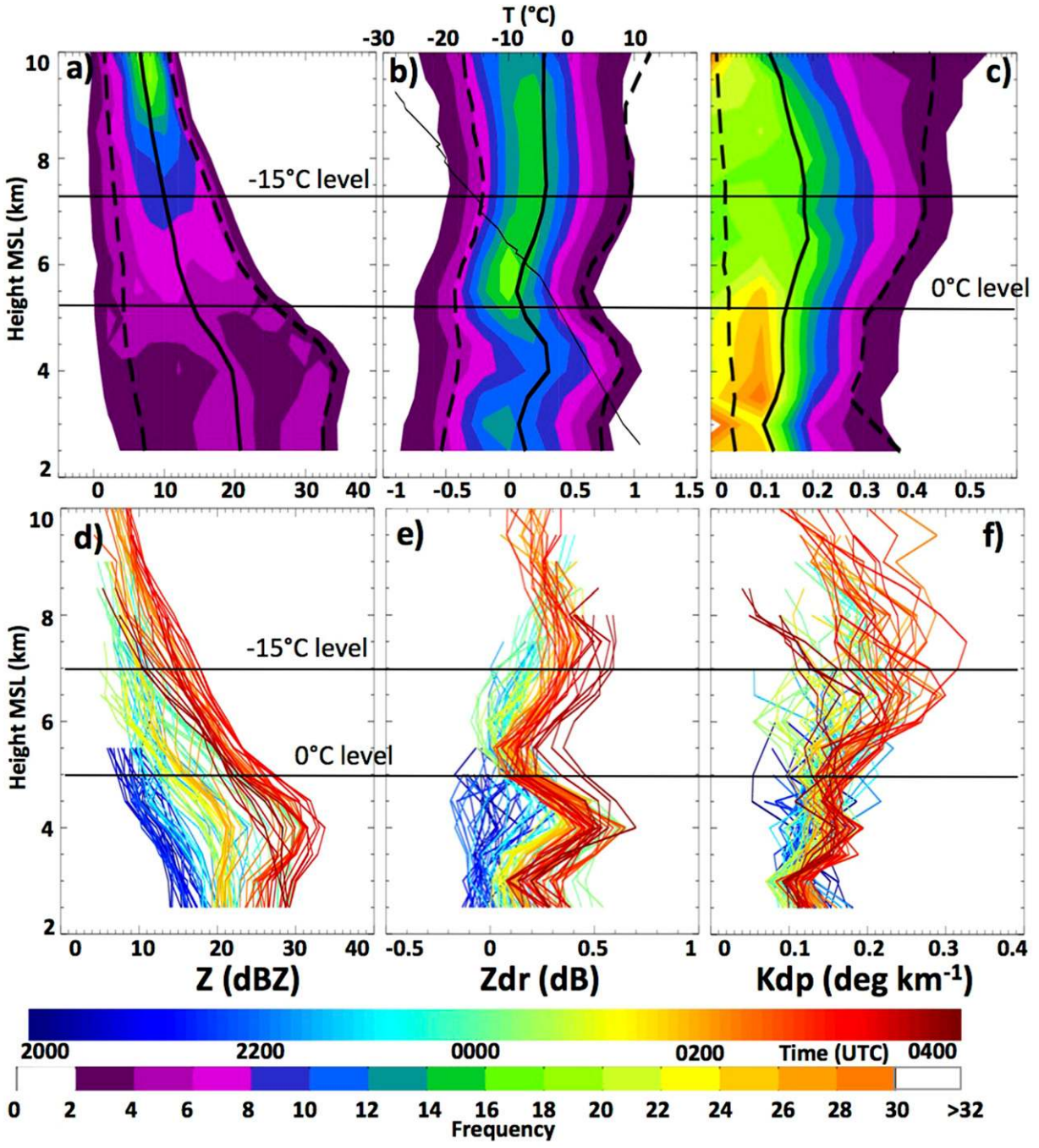

FIG. 15. As in Fig. 11, but only for the second episode between 2000 and 0400 UTC 12–13 Sep. The radar analyses for the plains and foothills were computed over the 62-km domains displayed in Fig. 1b (red box) and Fig. 2 (black box).

5. Vertical structure of clouds and precipitation at instrument sites

Large variations in the vertical extent of the clouds were observed during the first and second episodes, as shown in radar reflectivity over the CU campus (Fig. 17) and the Sugarloaf site (Fig. 18). As discussed in section 4, the first episode was dominated by convective rain, whereas the second episode had characteristics of both convective and stratiform rain. The rainfall is classified as shallow and deep convective during the first episode and stratiform–convective during the second episode based on the vertical structure of Z. In addition, rainfall entirely produced below the 0°C level, similar to the

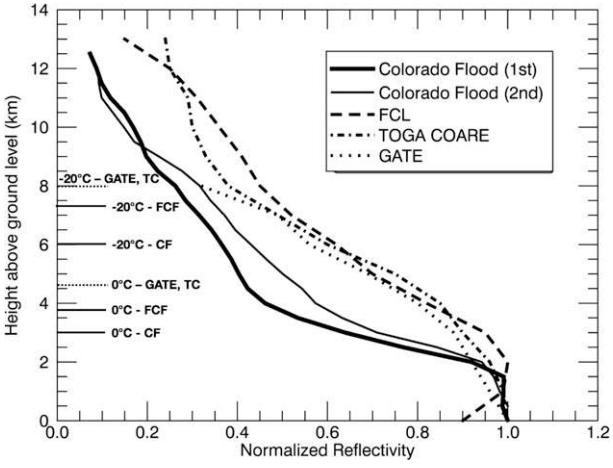

FIG. 16. Normalized mean reflectivity as a function of height for the first and second episodes of intense rainfall during the Colorado Flood (thick and thin solid lines), the 1997 Fort Collins flood (FCL, dashed line; Petersen et al. 1999), TOGA COARE (dashed–dotted line; DeMott and Rutledge 1998), and GATE (dotted line; Szoke and Zipser 1986). Values for FCL, TOGA COARE, and GATE were derived from Fig. 16 in Petersen et al. (1999). Horizontal solid (dotted) lines indicate the height of the 0° and −20°C level for the Colorado Flood (CF) and FCL [TOGA COARE (TC) and GATE].

rainfall described as nonbrightband rain by White et al. (2003), was observed at the end of the first episode. Further explanations will be given in the following paragraphs.

During shallow convective rain on 12 September, cloud tops were low (slightly above the 0°C level) and rain originated and grew at and below the melting layer, generating localized intense surface rainfall >50 mm h^{-1} both at the CU campus and Sugarloaf (Figs. 17a, 18a). Frequency analysis of reflectivity observed by the KFTG radar and Doppler velocity observed by the MRR at the CU campus site (Figs. 19a,b) and Marshall site (Figs. 20a,b) also support the rapid growth of particles, in particular between 4 and 5 km MSL. Reflectivity and Doppler velocity rapidly increased with decreasing height between 3.5 and 5 km (i.e., below the 0°C level) from 22 to 35 dBZ (10–20 dBZ) and from 3 to 6 m s^{-1} (2–4 m s^{-1}) at the CU campus (Marshall). Assuming this layer had a large number of liquid water drops and the Doppler velocity measured by the MRR is equal to the particle fall velocity, the increase in Doppler velocity at the CU campus during this time would relate to an increase in drop diameter by 1 mm (0.7–1.7 mm) when applying the Gunn and Kinzer (1949) relationship between average fall velocity and raindrop diameter. Between the surface and 3.5 km MSL, the reflectivity only slightly increased by 3 dB over 1.5 km while the Doppler velocity remained almost steady at 6 m s^{-1} at the CU campus. Drop diameters observed by the disdrometer at the surface ranged between 1.0 and 1.5 mm (Gochis et al. 2015). Because of the high moisture content and small drop sizes close to the surface, it can be

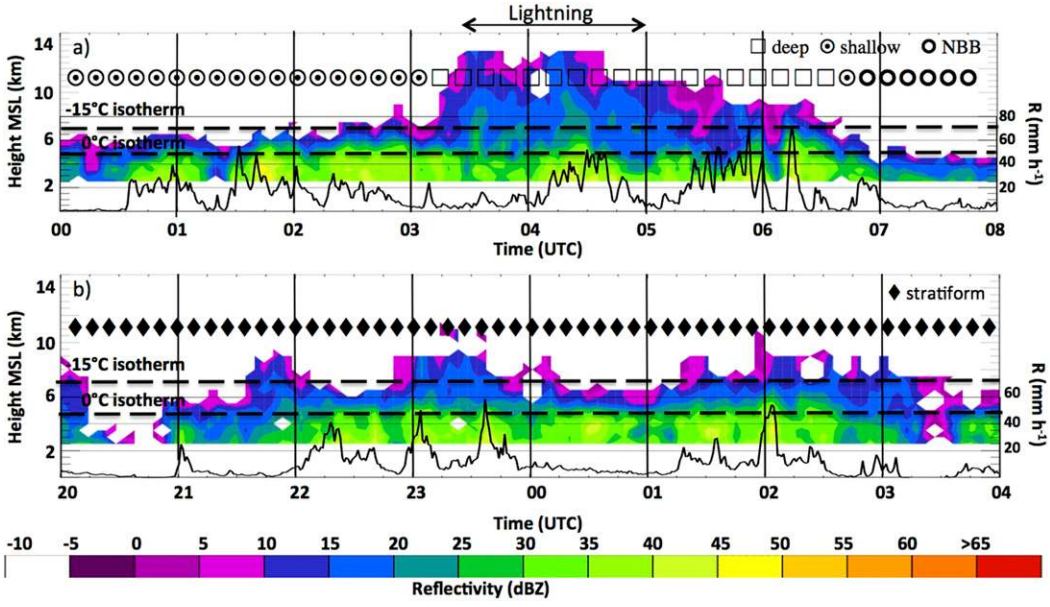

FIG. 17. Vertical profile of reflectivity (color coded) based on the KFTG radar data and disdrometer-derived rainfall rate (solid black lines) at the CU campus during the (a) first and (b) second episodes. Dashed lines indicate the 0° and −15°C levels, respectively. Rainfall type classification is shown, with squares, filled circles, empty circles, and diamond symbols denoting deep convective, shallow convective, nonbrightband, and stratiform–convective rain, respectively. Time period associated with electrical activity is indicated in (a).

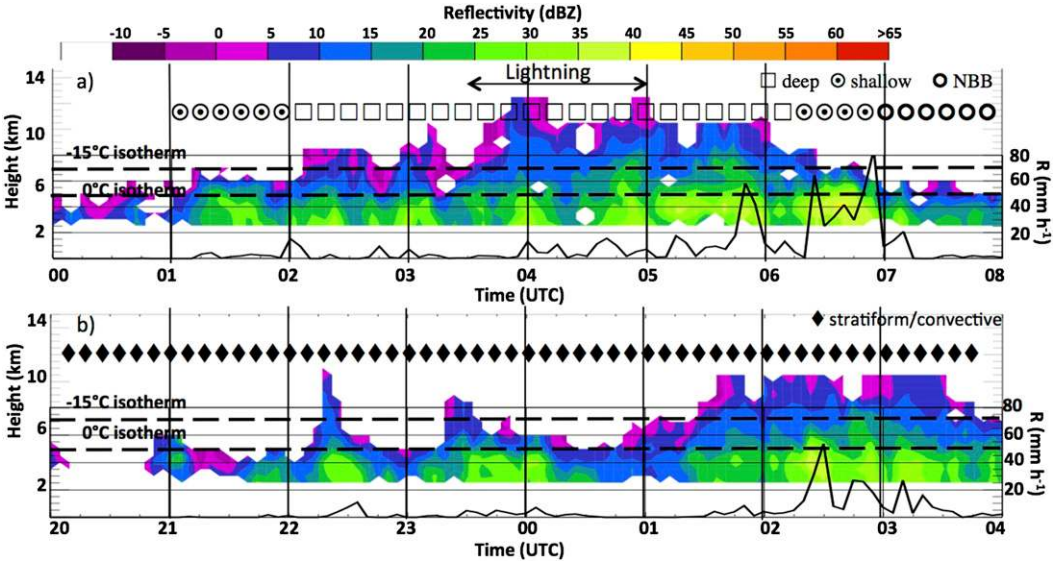

FIG. 18. As in Fig. 17, but for the Sugarloaf site.

assumed that evaporation and raindrop breakup were negligible. Below 4 km MSL, the increase in mean reflectivity with decreasing height indicates continuous growth through collision–coalescence, while the varying Doppler velocities were also associated with variations in the vertical velocity. The PID algorithm shown in Fig. 21a indicates that during shallow convective rain, ice crystals and dry snow were present 30%–40% of the time between 5 and 8 km MSL. Wet snow was occasionally observed above the 0°C level between 5 and 6 km MSL. Below the 0°C level, light and moderate rain were dominant, with melting wet snow between 3 and 4 km MSL. Note that the microwave radiometer indicated the presence of supercooled liquid after 0230 UTC. However, lightning activity at Sugarloaf and the CU campus did not start until ~0330 UTC (Fig. 13).

Later on, when the convergence zones associated with the mesoscale circulation interacted with the terrain (0315–0645 UTC), the vertical extent of the clouds increased significantly. The clouds reached up to $T \sim -15°C$ ($z > 7$ km), where enhanced dendritic ice crystal production occurred (section 4b). This rainfall type is referred to as deep convective rain, which was only observed at the CU campus site and the mountain stations but not at Marshall. While rainfall rates extended up to 80 mm h^{-1} at the CU campus, rainfall rates at Sugarloaf were much lower compared to the CU campus (Figs. 3b, 18a). Supercooled liquid was observed at the CU campus by the microwave radiometer until 0400 UTC. Lightning at Sugarloaf and Melvina Hill indicating the presence of graupel was observed until 0430 UTC. Rainfall at Sugarloaf peaked only at 0555 UTC with $R \sim 55$ mm h^{-1}, when the mesoscale circulation approached the mountains. Based on the reflectivity CFAD shown in Fig. 19c, reflectivity steadily increased from 12 to 22 dBZ between 4 and 6.5 km at the CU campus, which might be related to melting and rapid particle growth. Below the 0°C level (4–5 km), reflectivity and Doppler velocity increased rapidly with decreasing height (Figs. 19c,d). While the reflectivity values at 4 km are only slightly smaller during deep convective rain compared to shallow convective rain, the Doppler velocities measured by the MRR at 4 km were much slower, with 4.5 m s^{-1} during deep convective rain compared to ~6 m s^{-1} during shallow convective rain. Assuming that the MRR Doppler velocity is close to the raindrop fall velocity, 4.5 m s^{-1} (6 m s^{-1}) fall velocity would relate to raindrops with 1.16 mm (1.75 mm) diameter following Gunn and Kinzer (1949). Below 4 km MSL, a steady increase in reflectivity and Doppler velocity was observed, leading to the assumption that raindrops continued to grow by collision–coalescence during this time. However, the slower Doppler velocity during deep convective compared to shallow convective rain might be also associated with stronger updrafts. The PID algorithm based on KFTG radar parameters shown in Fig. 21b indicated large amounts of dry snow and ice crystals above the 0°C level during deep convective rain, melting into wet snow and rain below the melting layer.

Relatively small rainfall rates were observed during nonbrightband rain at the CU campus (Sugarloaf) with <10 mm h^{-1} (20 mm h^{-1}; Figs. 17a, 18a) after 0700 UTC. Compared to shallow convective rain, radar echoes ($Z > 0$ dBZ) only occurred below the 0°C level during nonbrightband rain. We can assume that during both shallow convective and nonbrightband rain, warm

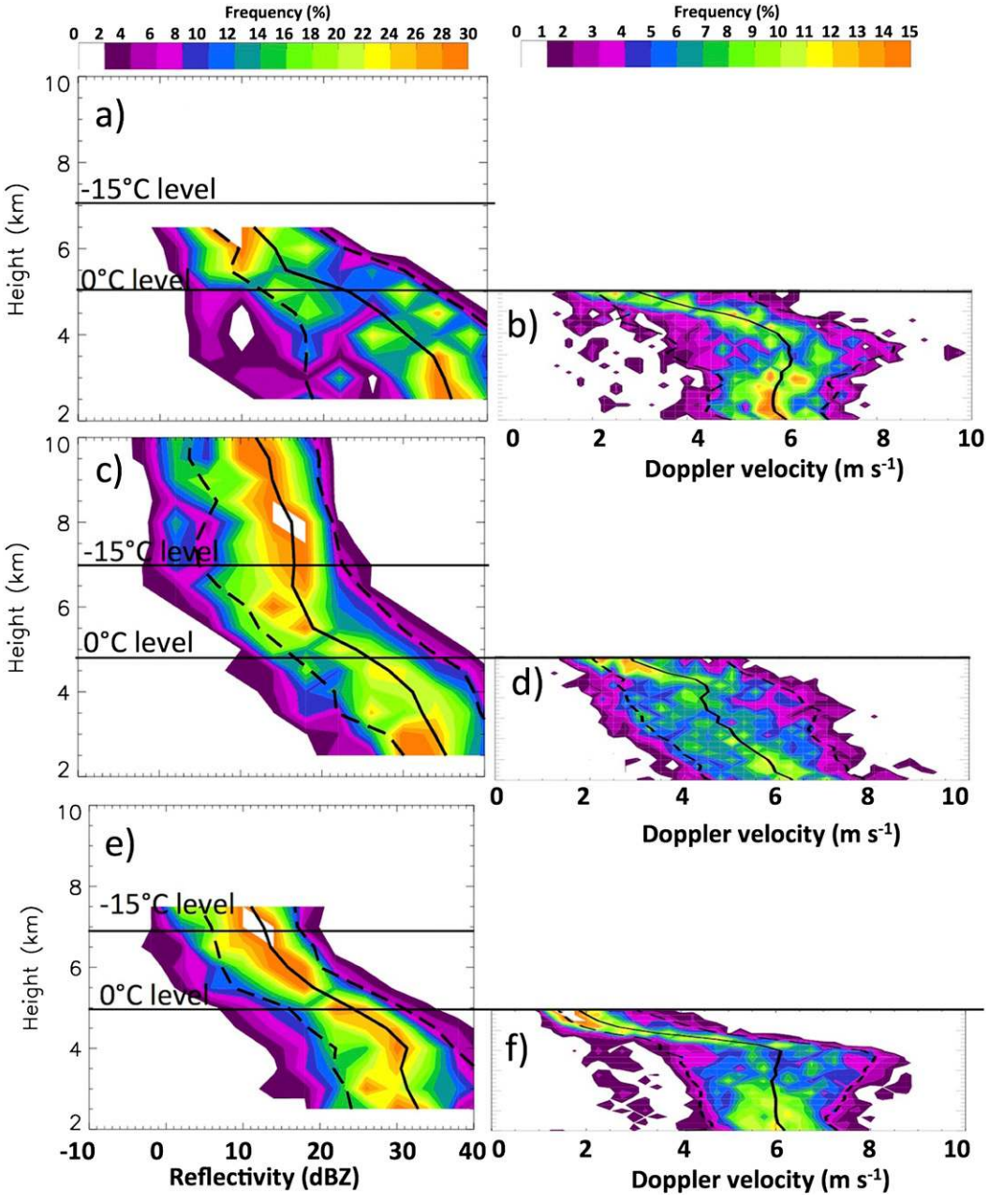

FIG. 19. Frequency distributions as a function of height for (left) reflectivity based on the KFTG data and (right) Doppler velocity based on the CU campus MRR data: (a),(b) shallow convective; (c),(d) deep convective; and (e),(f) stratiform–convective rain. Positive Doppler velocity values indicate downward motion. Solid black lines indicate the median value, and dashed black lines indicate the 10th and 90th percentiles, respectively.

rain processes dominated, since most of the increase in reflectivity and Doppler velocity occurred at and below the 0°C level and no significant lightning activity or supercooled liquid water were observed during those times. In addition, the reflectivity and Doppler velocity profiles during shallow convective and nonbrightband rain are similar to those observed along the coast of California during nonbrightband events (White et al. 2003), with the largest reflectivity values observed close to the ground and a steep increase in reflectivity with decreasing height (>15 dB km^{-1}) below the 0°C level (see also Fig. 11d).

During the second episode, a mixture of stratiform rain with a melting layer between 4 and 5 km MSL and convective rain was observed at the CU campus and Sugarloaf (Figs. 17b, 18b). The vertical extent of the

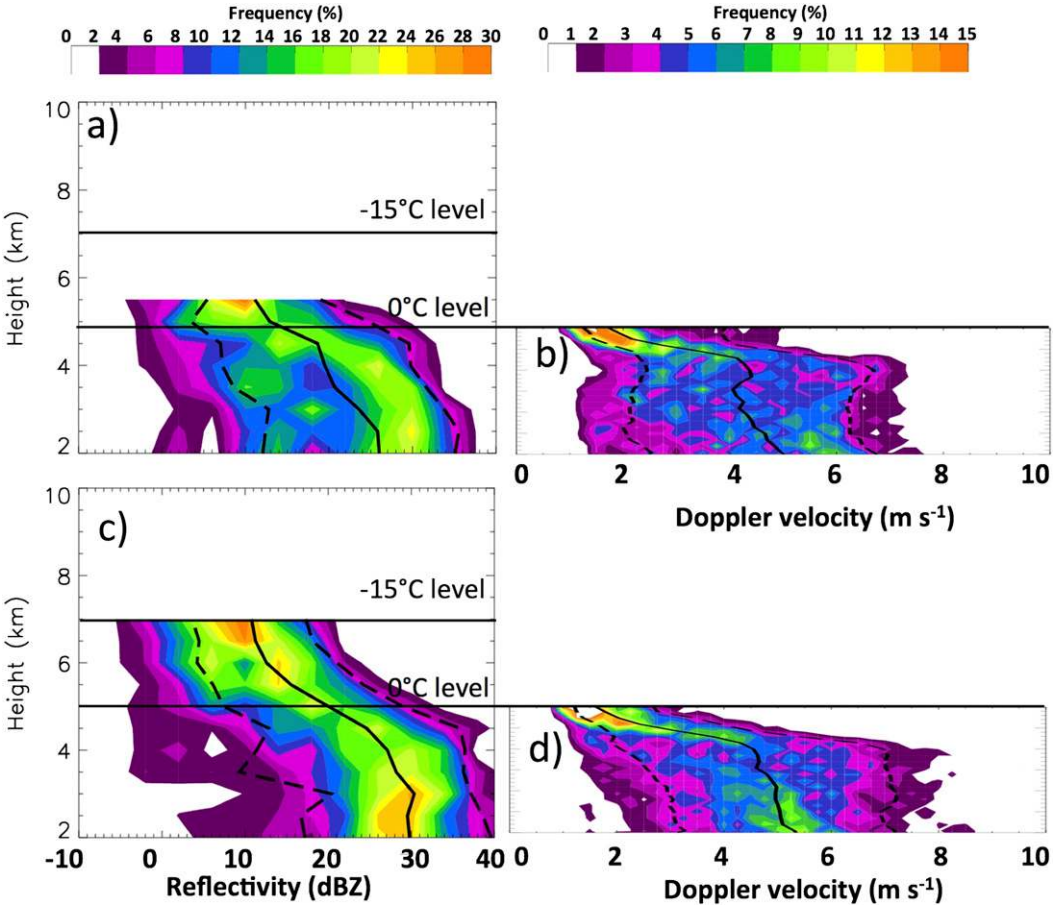

FIG. 20. As in Fig. 17, but for the Marshall site during (a),(b) shallow convective and (c),(d) stratiform–convective rain.

clouds varied from reaching slightly above the 0°C level to times when the clouds exceeded the −15°C temperature level. At the CU campus, enhancement in radar reflectivity at and below the 0°C level was most likely associated with more intense vertical lift, and embedded convection was occasionally observed (e.g., 2215–2245, 2300–2310, and 0015–0115 UTC) with large rainfall rates of $>20\,\mathrm{mm\,h^{-1}}$ (e.g., ~2100 and 2215–2245 UTC). We refer to this rainfall type as stratiform–convective rain. Enhanced liquid water ($\sim 0.4\,\mathrm{g\,m^{-3}}$) above the 0°C level was observed between 2200 and 0000 UTC by the microwave radiometer (figure not shown). No lightning was observed during the second episode. Frequency analyses of reflectivity and Doppler velocity at the CU campus and Marshall show a strong increase in reflectivity and Doppler velocity with decreasing height between 4 and 6 km, similar to the features observed during convective rain. The PID algorithm (Fig. 21c) identified irregular ice crystals and occasionally dry snow above 7 km with wet snow above and below the 0°C level. Ice crystal and dry snow frequencies were smaller compared to the convective times. Below 4 km MSL, light rain was identified by the PID algorithm with little change in the Doppler velocity and reflectivity values.

6. Conclusions

Cloud and precipitation structures during times of intense rainfall between 11 and 13 September during the 2013 Great Colorado Flood have been examined using the operational sounding and the dual-polarization Doppler weather radar at Denver, the Colorado Lightning Mapping Array, two vertically pointing micro rain radars, and four surface disdrometers. The investigation was divided into three parts: 1) the spatial and temporal evolution of clouds and precipitation, 2) the vertical structure of clouds and precipitation over the foothills, and 3) the vertical structure of clouds and precipitation across the foothills comparing lower-elevation stations with higher-elevation stations. Intense rainfall was characterized by shallow and deep convection within

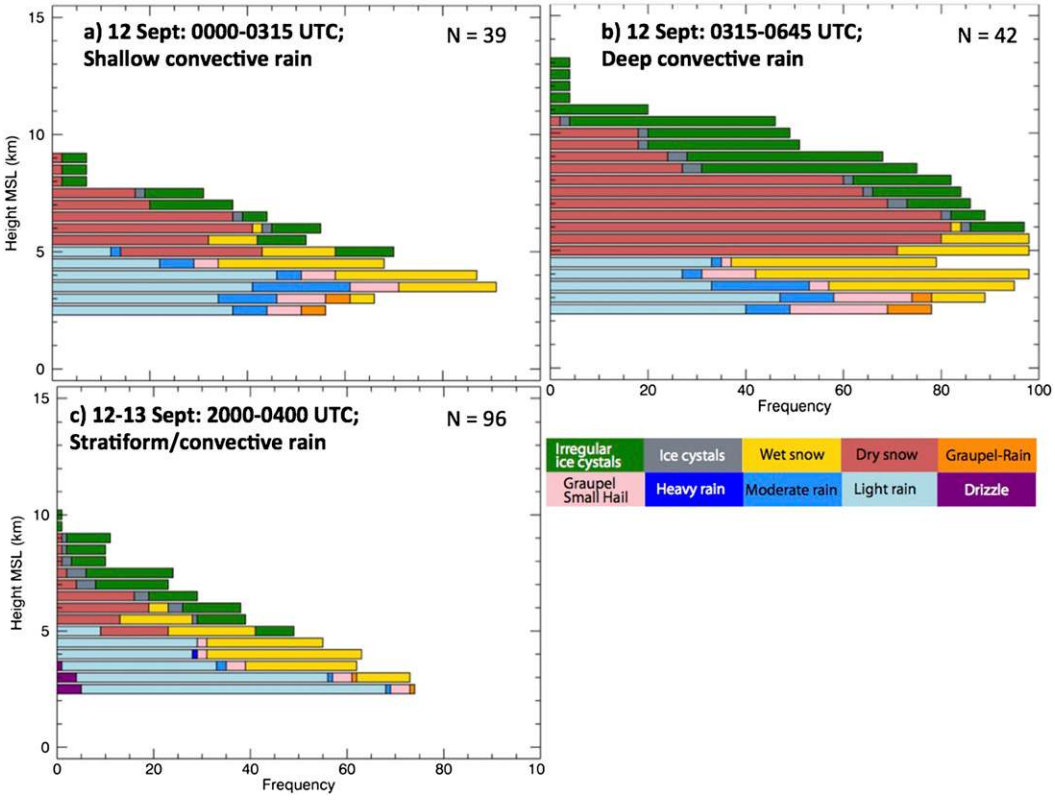

FIG. 21. As in Fig. 12, but for the rain types observed on the CU campus: (a) shallow convective rain, (b) deep convective rain, and (c) stratiform–convective rain. The number of time steps included in the analysis is indicated in the upper right corner.

stratiform rain occurring over the foothills between 0000 and 0800 UTC 12 September (first episode) and orographic rainfall over the foothills between 2200 and 0400 UTC 12–13 September (second episode).

Intense rainfall associated with orographic enhancement occurred during strong low-level easterly flow along the lower Colorado Front Range around 2 km MSL. In addition to orographic enhancement, the first episode was characterized by convective enhancement most likely triggered by surface mesoscale features. A mesoscale circulation accompanied by bands of enhanced convergence at the surface triggered deep convective clouds and intense rainfall in the Boulder area and, to a lesser extent, later on in the foothills as the circulation extended toward the mountains. Collision–coalescence and, to a lesser extent, riming can be considered the main microphysical processes during the times with shallow convective clouds at the beginning of the first episode. As the vertical extent of the clouds deepened beyond the −15°C level (deep convective rain), enhanced dendritic growth and, occasionally, aggregation might also have shaped the raindrop size distribution in addition to collision–coalescence and riming. Lightning and supercooled liquid water were observed during the transition from shallow to deep convective rain. Because of the high liquid water content and the small raindrop sizes ($d \sim 1$ mm), evaporation and raindrop breakup were less likely to occur. Medium Z and small Z_{dr} values, together with large rainfall rates, support the existence of small but numerous raindrops.

During the second episode, orographic enhancement over the foothills dominated and resulted in a mixture of stratiform and convective precipitation with a melting layer and embedded convective cells. Rainfall rates, mostly smaller than during the first episode, revealed that rain occurred in several short episodes of intense rainfall. All clouds during the second episode extended beyond the 0°C level, at times just 1–2 km above this level and at other times up to 9 km beyond the 0°C level. Enhanced supercooled liquid but no lightning was observed during the beginning of the second episode (2000–2350 UTC 12 September), which was more convective in nature compared to the end of the second episode. Enhanced dendritic growth was observed after 0000 UTC 13 September.

Based on the limited analysis of radar data and rainfall, the vertical structure of clouds and precipitation within the foothills strongly depended on the location of

the mesoscale features, that is, moisture flux and vertical velocity. During the first episode, intense rainfall occurred over Boulder close to the area of strongest wind shear. Marshall, only 5 km south of Boulder, received much less rainfall since it was located just south of the convergence zone. The vertical structure of reflectivity suggests that vertical lift was less at Marshall compared to the CU campus. While it is unclear how exactly the surface mesoscale features interacted with the terrain, the mesoscale circulation extended toward the mountains during a time when the rainfall increased. Rainfall at higher-elevation stations was much less compared to the lower-elevation stations. While the vertical extent of the clouds and the height of the 0°C isotherm were similar between the lower-and higher-elevation stations, the depth between 0°C isotherm and the surface (warm cloud depth) was reduced over the higher-elevation stations. As such, less rainfall occurred. A saturated layer of air up to 5 km and the small raindrop sizes observed at the surface suggest evaporation and drop breakup rarely occurred. It is unclear how much and how far moisture was transported into the mountains. While this study focused on the spatial and vertical distribution of rainfall, Friedrich et al. (2015) will analyze the rainfall size distributions between the lower and higher-elevation stations.

In summary, the microphysical processes are strongly linked to the low-level forcing. To predict the amount and distribution of rainfall accurately during events similar to the Great Colorado Flood, it is essential that numerical models are capable of reproducing the surface winds and mesoscale bands of convergence. Variations in vertical velocity and moisture flux due to terrain and low-level forcing triggered intense rainfall in very localized areas. Microphysical processes depend on the depth of the clouds with more warm-rain-dominated processes during times with shallow clouds and a combination of warm- and cold-rain processes during times with deeper clouds. Similarities in cloud and precipitation structures during the Great Colorado Flood were found with monsoon–ocean and tropical convection as well as coastal orographic rain. While warm-rain-dominated rainfall producing numerous small-sized raindrops has been observed in orographic rainfall, these conditions are rare in the dry continental climate in Colorado. However, the Great Colorado Flood has taught us that this kind of event can occur in Colorado with the right synoptic setup.

Acknowledgments. The authors thank the organizations, technicians, scientists, and students who support the instrument facilities that are used in this analysis. In particular, we thank Scott Kittelman, who maintains the instruments at the ATOC Skywatch observatory (skywatch.colorado.edu), the staff at the University of Colorado Mountain Research Station, and the staff at the NCAR Marshall facility. Thanks go to Drs. Paul Krehbiel and Bill Rison of New Mexico Tech and Wiebke Deierling of NCAR for providing the Colorado Lighting Mapping Array data. Critical comments provided by three anonymous reviewers led to substantial improvements in this manuscript. This work was supported in part by the U.S. National Science Foundation through its support of NCAR. Any opinions, findings, or recommendations expressed in this publication are those of the authors and do not necessarily reflect the views of the National Science Foundation.

REFERENCES

Andric, J., D. Zrnic, J. Straka, and V. Melnikov, 2010: The enhanced ZDR signature in stratiform clouds above melting layer. Preprints, *13th Conf. on Cloud Physics*, Portland, OR, Amer. Meteor. Soc., P2.89. [Available online at http://ams.confex.com/ams/pdfpapers/171308.pdf.]

Benavides-Solorio, J., and L. H. MacDonald, 2001: Post-fire runoff and erosion from simulated rainfall on small plots, Colorado Front Range. *Hydrol. Processes*, **15**, 2931–2952, doi:10.1002/hyp.383.

Caracena, F., R. A. Maddox, L. R. Hoxit, and C. F. Chappell, 1979: Mesoanalysis of the Big Thompson storm. *Mon. Wea. Rev.*, **107**, 1–17, doi:10.1175/1520-0493(1979)107<0001:MOTBTS>2.0.CO;2.

Collins, D. L., N. J. Doesken, and W. P. Stanton, 1991: Colorado floods and droughts. National Water Summary 1988–89: Hydrologic events and floods and droughts, USGS Water Supply Paper 2375, R. W. Paulson et al., Eds., U S. Dept. of the Interior, 207–214. [Available online at http://pubs.er.usgs.gov/publication/wsp2375.]

DeMott, C. A., and S. A. Rutledge, 1998: The vertical structure of TOGA COARE convection. Part I: Radar echo distributions. *J. Atmos. Sci.*, **55**, 2730–2747, doi:10.1175/1520-0469(1998)055<2730:TVSOTC>2.0.CO;2.

Friedrich, K., S. Higgins, F. J. Masters, and C. R. Lopez, 2013a: Articulating and stationary PARSIVEL disdrometer in severe weather. *J. Atmos. Oceanic Technol.*, **30**, 2063–2080, doi:10.1175/JTECH-D-12-00254.1.

——, E. A. Kalina, F. J. Masters, and C. R. Lopez, 2013b: Drop-size distributions in thunderstorms measured by optical disdrometers during VORTEX2. *Mon. Wea. Rev.*, **141**, 1182–1203, doi:10.1175/MWR-D-12-00116.1.

——, ——, J. Aikins, D. Gochis, K. Ikeda, P. Kucera, and M. Steiner, 2015: Raindrop size distribution and rain characteristics during the 2013 Great Colorado Flood. *J. Hydrometeor.*, **17**, 53–72, doi:10.1175/JHM-D-14-0184.1.

Gochis, D., and Coauthors, 2015: The Great Colorado Flood of September 2013. *Bull. Amer. Meteor. Soc.*, doi:10.1175/BAMS-D-13-00241.1, in press.

Godt, J. W., and J. A. Coe, 2007: Alpine debris flows triggered by a 28 July 1999 thunderstorm in the central Front Range, Colorado. *Geomorphology*, **84**, 80–97, doi:10.1016/j.geomorph.2006.07.009.

Goodman, S. J., and H. J. Christian, 1993: Global observations of lightning. *Global Change Atlas*, R. Gurney, J. Foster, and C. Parkinson, Eds., Cambridge University Press, 325–355.

Gunn, R., and G. D. Kinzer, 1949: The terminal velocity of fall for water droplets in stagnant air. *J. Meteor.*, **6**, 243–248, doi:10.1175/1520-0469(1949)006<0243:TTVOFF>2.0.CO;2.

Heggli, M. F., and R. M. Rauber, 1988: The characteristics and evolution of supercooled water in wintertime storms over the Sierra Nevada: A summary of microwave radiometric measurements taken during the Sierra cooperative pilot project. *J. Appl. Meteor.*, **27**, 989–1015, doi:10.1175/1520-0450(1988)027<0989:TCAEOS>2.0.CO;2.

Hirschboeck, K. K., 1991: Climate and floods. National Water Summary 1988–89: Hydrologic events and floods and droughts, USGS Water Supply Paper 2375, R. W. Paulson et al., Eds., U.S. Dept. of the Interior, 67–88. [Available online at http://pubs.er.usgs.gov/publication/wsp2375.]

Houze, R. A., 1993: *Cloud Dynamics.* Academic Press, 573 pp.

Hubbert, J., and V. N. Bringi, 1995: An iterative filtering technique for the analysis of coplanar differential phase and dual-frequency radar measurements. *J. Atmos. Oceanic Technol.*, **12**, 643–648, doi:10.1175/1520-0426(1995)012<0643:AIFTFT>2.0.CO;2.

Ikeda, K., R. M. Rasmussen, W. D. Hall, and G. Thompson, 2007: Observations of freezing drizzle in extratropical cyclonic storms during IMPROVE-2. *J. Atmos. Sci.*, **64**, 3016–3043, doi:10.1175/JAS3999.1.

International and Scientific Management Group for GATE, 1974: GATE. *Bull. Amer. Meteor. Soc.*, **55**, 711–744, doi:10.1175/1520-0477(1974)055<0711:G>2.0.CO;2.

Kennedy, P. C., and S. A. Rutledge, 2011: S-band dual-polarization radar observations of winter storms. *J. Appl. Meteor. Climatol.*, **50**, 844–858, doi:10.1175/2010JAMC2558.1.

Krehbiel, P. R., R. J. Thomas, W. Rison, T. Hamlin, J. Harlin, and M. Davis, 2000: GPS-based mapping system reveals lightning inside storms. *Eos, Trans. Amer. Geophys. Union*, **81**, 21–25, doi:10.1029/00EO00014.

Lang, T. S., S. A. Rutledge, B. Dolan, P. Krehbiel, W. Rison, and D. T. Lindsey, 2014: Lightning in wildfire smoke plumes observed in Colorado during summer 2012. *Mon. Wea. Rev.*, **142**, 489–507, doi:10.1175/MWR-D-13-00184.1.

Löffler-Mang, M., and J. Joss, 2000: An optical disdrometer for measuring size and velocity of hydrometeors. *J. Atmos. Oceanic Technol.*, **17**, 130–139, doi:10.1175/1520-0426(2000)017<0130:AODFMS>2.0.CO;2.

——, and U. Blahak, 2001: Estimation of the equivalent radar reflectivity factor from measured snow size spectra. *J. Appl. Meteor.*, **40**, 843–849, doi:10.1175/1520-0450(2001)040<0843:EOTERR>2.0.CO;2.

——, M. Kunz, and W. Schmid, 1999: On the performance of a low-cost K-band Doppler radar for quantitative rain measurement. *J. Atmos. Oceanic Technol.*, **16**, 379–387, doi:10.1175/1520-0426(1999)016<0379:OTPOAL>2.0.CO;2.

Maddox, R. A., F. Caracena, L. R. Hoxit, and C. F. Chappell, 1977: Meteorological aspects of the Big Thompson flash flood of 31 July 1976. NOAA Tech. Rep. ERL 388-APCL 41, 88 pp.

——, L. R. Hoxit, C. F. Chappell, and F. Caracena, 1978: Comparison of meteorological aspects of the Big Thompson and Rapid City flash floods. *Mon. Wea. Rev.*, **106**, 375–389, doi:10.1175/1520-0493(1978)106<0375:COMAOT>2.0.CO;2.

Marwitz, J. D., 1987: Deep orographic storms over the Sierra Nevada. Part I: Thermodynamic and kinematic structure. *J. Atmos. Sci.*, **44**, 159–173, doi:10.1175/1520-0469(1987)044<0159:DOSOTS>2.0.CO;2.

McKee, T. B., and N. J. Doesken, 1997: Final report: Colorado extreme precipitation data study. Climatology Rep. 97-1, Dept. of Atmospheric Science, Colorado State University, 107 pp. [Available online at http://ccc.atmos.colostate.edu/pdfs/Climo_97-1_Extreme_ppt.pdf.]

Moody, J. A., and D. A. Martin, 2001: Initial hydrologic and geomorphic response following a wildfire in the Colorado Front Range. *Earth Surf. Processes Landforms*, **26**, 1049–1070, doi:10.1002/esp.253.

OFCM, 2006: Doppler radar meteorological observations: Part C, WSR-88D products and algorithms. Federal Meteorological Handbook 11, Rep. FCM-H11C-2006, Dept. of Commerce, 5-1–5-23. [Available online at http://www.ofcm.gov/fmh11/fmh11C.htm.]

Orville, R. E., and R. W. Henderson, 1986: Global distribution of midnight lightning: December 1997 to August 1978. *Mon. Wea. Rev.*, **114**, 2640–2653, doi:10.1175/1520-0493(1986)114<2640:GDOMLS>2.0.CO;2.

Peters, G., B. Fischer, and T. Andersson, 2002: Rain observations with a vertically looking Micro Rain Radar (MRR). *Boreal Environ. Res.*, **7**, 353–362.

——, ——, H. Münster, M. Clemens, and A. Wagner, 2005: Profiles of raindrop size distributions as retrieved by microrain radars. *J. Appl. Meteor.*, **44**, 1930–1949, doi:10.1175/JAM2316.1.

Petersen, W. A., and Coauthors, 1999: Mesoscale and radar observations of the Fort Collins flash flood of 28 July 1997. *Bull. Amer. Meteor. Soc.*, **80**, 191–216, doi:10.1175/1520-0477(1999)080<0191:MAROOT>2.0.CO;2.

Rauber, R. M., and L. O. Grant, 1986: The characteristics and distribution of cloud water over the mountains of northern Colorado during wintertime storms. Part II: Spatial distribution and microphysical characteristics. *J. Climate Appl. Meteor.*, **25**, 489–504, doi:10.1175/1520-0450(1986)025<0489:TCADOC>2.0.CO;2.

——, and ——, 1987: Supercooled liquid water structure of a shallow orographic cloud system in southern Utah. *J. Climate Appl. Meteor.*, **26**, 208–215, doi:10.1175/1520-0450(1987)026<0208:SLWSOA>2.0.CO;2.

——, ——, D. X. Feng, and J. B. Snider, 1986: The characteristics and distribution of cloud water over the mountains of northern Colorado during wintertime storms. Part I: Temporal variations. *J. Climate Appl. Meteor.*, **25**, 468–488, doi:10.1175/1520-0450(1986)025<0468:TCADOC>2.0.CO;2.

Rison, W., R. J. Thomas, P. R. Krehbiel, T. Hamlin, and J. Harlin, 1999: A GPS-based three-dimensional Lightning Mapping System: Initial observations in central New Mexico. *Geophys. Res. Lett.*, **26**, 3573–3576, doi:10.1029/1999GL010856.

——, P. R. Krehbiel, R. J. Thomas, D. Rodeheffer, and B. Fuchs, 2012: The Colorado Lightning Mapping Array. *2012 Fall Meeting*, San Francisco, CA, Amer. Geophys. Union, Abstract AE23B-0319.

Rollenbeck, R., J. Bendix, P. Fabian, J. Boy, W. Wilcke, H. Dalitz, M. Oesker, and P. Emck, 2007: Comparison of different techniques for the measurement of precipitation in tropical montane rain forest regions. *J. Atmos. Oceanic Technol.*, **24**, 156–168, doi:10.1175/JTECH1970.1.

Rutledge, S. A., E. R. Williams, and D. Keenan, 1992: The Down Under Doppler and Electricity Experiment (DUNDEE): Overview and preliminary results. *Bull. Amer. Meteor. Soc.*, **73**, 3–16, doi:10.1175/1520-0477(1992)073<0003:TDUDAE>2.0.CO;2.

Ryzhkov, A. V., D. S. Zrnic, and B. A. Gordon, 1998: Polarimetric method for ice water content determination. *J. Appl.*

Meteor., **37**, 125–134, doi:10.1175/1520-0450(1998)037<0125:PMFIWC>2.0.CO;2.

Srivastava, R. C., 1971: Size distribution of raindrops generated by their breakup and coalescence. *J. Atmos. Sci.*, **28**, 410–415, doi:10.1175/1520-0469(1971)028<0410:SDORGB>2.0.CO;2.

Sun, J., and N. A. Crook, 1997: Dynamical and microphysical retrieval from Doppler radar observations using a cloud model and its adjoint. Part I: Model development and simulated data experiments. *J. Atmos. Sci.*, **54**, 1642–1661, doi:10.1175/1520-0469(1997)054<1642:DAMRFD>2.0.CO;2.

Sveinsson, O., J. Salas, and D. Boes, 2002: Regional frequency analysis of extreme precipitation in northeastern Colorado and Fort Collins Flood of 1997. *J. Hydrol. Eng.*, **7**, 49–63, doi:10.1061/(ASCE)1084-0699(2002)7:1(49).

Szoke, E. J., and J. Zipser, 1986: A radar study of convective cells in mesoscale systems in GATE. Part II: Life cycles of convective cells. *J. Atmos. Sci.*, **43**, 199–218, doi:10.1175/1520-0469(1986)043<0199:ARSOCC>2.0.CO;2.

Thomas, R. J., P. R. Krehbiel, W. Rison, T. Hamlin, J. Harlin, and D. Shown, 2001: Observations of VHF source powers radiated by lightning. *Geophys. Res. Lett.*, **28**, 143–146, doi:10.1029/2000GL011464.

Tokay, A., P. Hartmann, A. Battaglia, K. S. Gage, W. L. Clark, and C. R. Williams, 2009: A field study of reflectivity and *Z–R* relations using vertically pointing radars and disdrometers. *J. Atmos. Oceanic Technol.*, **26**, 1120–1134, doi:10.1175/2008JTECHA1163.1.

Trapp, J. R., D. M. Schultz, A. V. Ryzhkov, and R. L. Holle, 2001: Multiscale structure and evolution of an Oklahoma winter precipitation event. *Mon. Wea. Rev.*, **129**, 486–501, doi:10.1175/1520-0493(2001)129<0486:MSAEOA>2.0.CO;2.

Trivej, P., and B. Stevens, 2010: The echo size distribution of precipitation shallow cumuli. *J. Atmos. Sci.*, **67**, 788–804, doi:10.1175/2009JAS3178.1.

Vivekanandan, J., D. S. Zrnic, S. M. Ellis, R. Oye, A. V. Ryzhkov, and J. Straka, 1999: Cloud microphysics retrieval using S-band dual-polarization radar measurements. *Bull. Amer. Meteor. Soc.*, **80**, 381–388, doi:10.1175/1520-0477(1999)080<0381:CMRUSB>2.0.CO;2.

Wagenbrenner, J. W., L. H. MacDonald, and D. Rough, 2006: Effectiveness of three post-fire rehabilitation treatments in the Colorado Front Range. *Hydrol. Processes*, **20**, 2989–3006, doi:10.1002/hyp.6146.

Weaver, J. F., E. Gruntfest, and G. M. Levy, 2000: Two floods in Fort Collins, Colorado: Learning from a natural disaster. *Bull. Amer. Meteor. Soc.*, **81**, 2359–2366, doi:10.1175/1520-0477(2000)081<2359:TFIFCC>2.3.CO;2.

Webster, P. J., and R. Lukas, 1992: TOGA COARE: The Coupled Ocean–Atmosphere Response Experiment. *Bull. Amer. Meteor. Soc.*, **73**, 1377–1416, doi:10.1175/1520-0477(1992)073<1377:TCTCOR>2.0.CO;2.

White, A. B., P. J. Neiman, F. M. Ralph, D. E. Kingsmill, and P. O. G. Persson, 2003: coastal orographic rainfall processes observed by radar during the California land-falling jets experiment. *J. Hydrometeor.*, **4**, 264–282, doi:10.1175/1525-7541(2003)4<264:CORPOB>2.0.CO;2.

Wiens, K. C., S. A. Rutledge, and S. A. Tessendorf, 2005: The 29 June 2000 supercell observed during STEPS. Part II: Lightning and charge structure. *J. Atmos. Sci.*, **62**, 4151–4177, doi:10.1175/JAS3615.1.

Williams, E. R., S. A. Rutledge, S. G. Geotis, N. Renno, E. Rasmussen, and T. Rickenbach, 1992: A radar and electrical study of tropical "hot towers." *J. Atmos. Sci.*, **49**, 1386–1395, doi:10.1175/1520-0469(1992)049<1386:ARAESO>2.0.CO;2.

Yuter, S. E., and R. A. Houze Jr., 1995: Three-dimensional kinematic and microphysical evolution of Florida cumulonimbus. Part II: Frequency distributions of vertical velocity, reflectivity, and differential reflectivity. *Mon. Wea. Rev.*, **123**, 1941–1963, doi:10.1175/1520-0493(1995)123<1941:TDKAME>2.0.CO;2.

Zipser, E. J., 1994: Deep cumulonimbus cloud systems in the tropics with and without lightning. *Mon. Wea. Rev.*, **122**, 1837–1851, doi:10.1175/1520-0493(1994)122<1837:DCCSIT>2.0.CO;2.

——, and K. R. Lutz, 1994: The vertical profile of radar reflectivity of convective cells: A strong indicator of storm intensity and lightning probability? *Mon. Wea. Rev.*, **122**, 1751–1759, doi:10.1175/1520-0493(1994)122<1751:TVPORR>2.0.CO;2.